Identification of multiple co-located hydrometeor types in Doppler spectra from scanning polarimetric cloud radar observations

Majid Hajipour [1], Patric Seifert [1], Hannes Griesche [1], Kevin Ohneiser [1], and Martin Radenz [1]

[1]Leibniz Institute for Tropospheric Research, Leipzig, Germany

Correspondence: Majid Hajipour (hajipour@tropos.de)

Abstract. To date, there remains a noticeable gap in reliable techniques for retrieving the shape and orientation of ice particles from observational data. This paper introduces a method using ground-based polarimetric cloud radar to retrieve the shape and orientation of multiple hydrometeor types within deep mixed-phase clouds. Building on the strong performance of an existing method, which is effective in retrieving the shape and orientation of pristine ice particles in stratiform clouds, we

5 extended this technique by analyzing the entire Doppler spectrum. The previously developed main-peak approach focuses on the maximum of the Doppler spectrum to retrieve the shape and orientation of the dominant hydrometeor types within stratiform clouds. In the extended technique, referred to as the spectrally resolved technique, the full Doppler spectrum is analyzed by dividing it into five parts, ultimately allowing the retrieval of five distinct hydrometeor types. In this study, we employed the technique for Range-Height Indicator (RHI) scans (ranging from $30\,°$ to $90\,°$ elevation) utilizing polarimetric Ka-band cloud

10 radar observations of differential reflectivity (ZDR) and correlation coefficient (RHV) across the entire Doppler spectrum. The potential of the improved approach is presented by means of two case studies. The first case demonstrates the effectiveness of the spectrally resolved approach and in the second case secondary ice production is investigated. These findings contribute to a profound understanding of hydrometeor characteristics, shedding light on dynamic cloud processes, especially in the context of precipitation and ice particle formation.

15 ## 1 Introduction

Integral to Earth's climate system, clouds play a crucial role in the global water cycle. Mixed-phase clouds, containing both liquid droplets and ice crystals (Korolev et al., 2017), are a major source of precipitation in mid-latitude regions (Mülmenstädt et al., 2015). These clouds can form within the temperature range from $-38\,°$C and $0\,°$C. Ice particles can form only at temperatures below $0\,°$C, while liquid droplets can exist in the atmosphere down to about $-38\,°$C. Ice particles can form via

20 several distinct ways, such as homogeneous ice formation (Austin and Jeffery, 1997), heterogeneous ice formation (Hoose and Möhler, 2012), or secondary ice production (SIP) (Korolev and Leisner, 2020). Consequence is, that usually, multiple hydrometeor types do co-exist in a cloud volume as long as the cloud system extends over a diverse range of temperature, humidity and dynamics.

In general, mixed-phase clouds can be categorized into deep or stratiform types based on their vertical extent. Deep clouds exhibit a distinct vertical structure, often resulting in complex aggregated or rimed ice crystals. In contrast, stratiform mixed-

phase clouds are characterized by a shallow layer, dominated by supercooled liquid droplets at the cloud top that contains predominantly pristine crystals which may precipitate further downward (Field et al., 2005; Zeng et al., 2023; Qi et al., 2019). Deep mixed-phase clouds display diverse microphysical processes that are affected by ambient temperature, pressure, and humidity as well as their dynamics-driven variability (Pruppacher et al., 1998). The microphysical processes within mixed-

30 phase clouds include coalescence, aggregation, riming, sublimation, crystal breakup, and melting, which influence the size, concentration, and chemical composition of ice crystals (Hallet and Mossop, 1974). Studying the complex shapes of ice crystals in various temperature and saturation environments is crucial for advancing our understanding of the microphysical processes within clouds (Matsuo and Fukuta, 1987; Guichard and Couvreux, 2017).

Ground-based radar measurements, particularly those utilizing polarimetric cloud radars, have been crucial in examining the

35 microphysical properties of ice crystals. Polarimetric cloud radars, especially at higher frequencies such as Ka-band or W-band, provide increased sensitivity to ice crystals, enhancing the remote sensing of cloud microphysical properties (Kollias et al., 2007; Küchler et al., 2017; Görsdorf et al., 2015). The differential depolarization and backscattering characteristics of incident electromagnetic waves caused by hydrometeors offers valuable insights into their phase, shape, aspect ratio, orientation, and bulk density. Cloud Doppler radars, introduced by Wakasugi et al. (1986), provide backscattered signal as function of Doppler

40 velocity referred to as the Doppler spectrum. As the terminal fall speed of ice particles depends on their size, mass, and shape (Mitchell, 1996; Bühl et al., 2019), the Doppler spectrum can be considered as a fingerprint of the cloud microphysical structure. Early work by Matrosov (1991) demonstrated the possibility to distinguish prolate-shaped scatterers from oblate ones based on the depolarization ratio's dependency on the elevation angle of the radar antenna. Melnikov and Straka (2013) further showed that assuming a spheroid shape model, a combined analysis of polarimetric variables could provide information

45 about ice particle habits. Matrosov (2020) expanded these efforts by evaluating the aspect ratio of ice hydrometeors in Arctic clouds using polarimetric radar-based retrievals, highlighting the potential to obtain information about particle growth and microphysics. Myagkov et al. (2016a) introduced an approach, hereafter denoted as main-peak approach, utilizing only the peak signal from the cloud radar Doppler spectrum at a range of elevation angles at a given height level to retrieve the shape and orientation of the dominant ice particle type through the analysis of backscatter intensity. This methodology involves

50 comparing elevation (range-height indicator, RHI) scans of observed differential reflectivity (ZDR) and correlation coefficient (RHV) of particles with simulated angular dependencies of ZDR and RHV. The resulting output consists of a pair of values: the polarizability ratio (density-weighted axis ratio) and the degree of orientation. The polarizability ratio indicates the shape, while the degree of orientation indicates the orientation. These values represent the best match between the measured and modeled angular dependencies of the polarimetric variables. The main-peak approach was demonstrated by Myagkov et al.

55 (2016b), to yield valuable information about the shape and orientation of primarily formed ice particles which formed in thin stratiform mixed-phase clouds. Since the polarizability ratio and degree of orientation are analytically defined, they can in principle be used in model-observations comparison studies. This was, e.g., recently done for the polarizability ratio by Welss et al. (2024). Since clouds typically contain a mixture of various hydrometeor types, even at small spatial scales, the main-peak approach is however insufficient for retrieving multiple hydrometeor types. Therefore, this approach needs to be extended to

60 account for the diverse compositions of clouds.

The measured polarimetric variables of Doppler cloud radars exhibit sensitivity to specific fall velocities and shapes of hydrometeors, allowing the identification of the ice particle types (Shupe et al., 2004; Luke et al., 2010; Verlinde et al., 2013; Kalesse et al., 2016; Kollias et al., 2016, 2007; Fukao and Hamazu, 2014; Radenz et al., 2019). Pristine ice particles predominantly are observed in the low Doppler velocity range (down to $0\,\mathrm{m\,s^{-1}}$), while heavily rimed or large aggregated ice particles tend to be situated in the high Doppler velocity range (frequently greater than $2\,\mathrm{m\,s^{-1}}$). This paper presents an extension of the main-peak approach, which involves analyzing five parts of the Doppler spectra observed over a range of elevation angles from 30 to $90\,^{\circ}$ to yield vertical profiles of polarizability ratio and degree of orientation as a function of Doppler velocity. To do so, cloud radar data from the ACCEPT (Analysis of the Composition of Clouds with Extended Polarization Techniques) campaign conducted in 2014 at Cabauw, Netherlands, will be analyzed and the potential of the proposed method will be highlighted. The whole cloud radar Doppler spectrum is utilized, with the goal of achieving a comprehensive retrieval of all hydrometeor types present in the clouds. In section 2, the instrumentation employed in this study is introduced. In section 3, we present a detailed exposition of the extended approach, providing insights into the enhancements made to the existing methodology. The practical application of the spectrally resolved approach is explored in section 4. Additionally, the capability of this approach to identify secondary ice production is investigated in a second case study, presenting its versatility in addressing different aspects of hydrometeor characterization within clouds.

2 Instrumentation

The ACCEPT measurement campaign, led by the Leibniz Institute for Tropospheric Research (TROPOS) in Leipzig, Germany, with partners from the Technical University of Delft and METEK GmbH in Elmshorn, Germany, aimed to explore the polarimetric capabilities of the MIRA-35 cloud radar. The campaign took place at the Cabauw Experimental Site for Atmospheric Research (CESAR) in the Netherlands from October 7 to November 18, 2014. Table 1 provides a comprehensive list of the instruments utilized specifically for this study. Two Doppler cloud radars of type Mira-35 (Görsdorf et al., 2015), were installed and operated during the campaign to cover different objectives. One MIRA-35 (MIRA-35 MBR4) configured in hybrid polarimetric mode (simultaneously transmitting and receiving signals across both horizontal and vertical channels.), was integrated into the LACROS (Leipzig Aerosol and Cloud Remote Observations System; Bühl et al., 2013) container at CESAR. It conducted 15-minute scanning cycles with two RHI scans per cycle, covering elevation angles from $30\,^{\circ}$ to $150\,^{\circ}$ at the two perpendicular oriented azimuth angles of $0\,^{\circ}$ (north-south) and $90\,^{\circ}$ (east-west). This system was in detail described by Myagkov et al. (2016a). The radar's accuracy was ensured through antenna coupling corrections and occasional calibration using light rain events (Myagkov et al., 2015, 2016a). Another MIRA-35 radar (MIRA-35 NMRA), with a linear depolarization configuration (LDR), operated simultaneously in continuous vertical-stare mode to observe cloud systems. To prevent interference, the two radars operated slightly at different frequencies (see Table 1) and were positioned 30 meters apart. A PollyXT multiwavelength Raman lidar (Engelmann et al., 2016) was used to detect supercooled liquid particles in mixed-phase clouds near the Cabauw meteorological tower. The lidar was strategically tilted by $5\,^{\circ}$ off-zenith to avoid specular reflection at the planar planes of horizontally oriented falling ice crystals (Westbrook et al., 2010). Cloud-top temperatures were determined

Table 1. Characteristics of the instruments employed during the ACCEPT campaign.

Instruments	Main specifications	Measurements	References
MIRA-35 NMRA	Frequency: 35.5 GHz configuration: LDR pointing: zenith temporal resolution: 1 s Range resolution: 30 m	Radar reflectivity factor LDR mean Doppler velocity Doppler width complete Doppler spectrum	Görsdorf et al. (2015)
MIRA-35 MBR4	Frequency: 35.17 GHz configuration: hybrid pointing: scanning temporal resolution: 1 s range resolution: 30 m	Radar reflectivity factor mean Doppler velocity Doppler width complete Doppler spectrum differential reflectivity correlation coefficient differential phase shift	Myagkov et al. (2016a)
Multiwavelength Raman lidar PollyXT	Wavelengths: 355 nm, 532 nm, 1064 nm pointing angle: 5 ° off-zenith temporal resolution: 30 s range resolution: 7.5 m	Backscatter coefficient, volume depolarization ratio	Althausen et al. (2009)
Microwave radiometer HATPRO	Bands: 22–31 GHz, 51–58 GHz temporal resolution: 1 s	Brightness temperatures temperature profile liquid water path integrated water vapor	Rose et al. (2005)
Radiosonde Vaisala RS92	Temporal resolution is fixed, range resolution can be estimaed by assuming an ascend speed of $5\,\mathrm{m\,s^{-1}}$	Temperature air pressure relative humidity horizontal wind vector	Suortti et al. (2008)

from the thermodynamic profiles of the atmosphere derived by various methods, including radiosondes, microwave radiometer,

95 and the GDAS1 model dataset, with priority on the first available dataset in the given order (Myagkov et al., 2016b).

The analysis was focused on mid-level mixed-phase clouds by meeting specific criteria, including the operation of the MIRA-35 MBR4, availability of calibrated polarimetric variables, and cloud-top temperatures ranging from approximately $-20°$ to $0°$C. The goal was to study ice crystal properties in non-precipitating cases, considering the shape retrieval algorithm's assumptions.

2.1 Mira-35 radar in hybrid mode

METEK GmbH, based in Elmshorn, Germany, manufactures the widely-used MIRA-35 cloud radar operating at 35 GHz. It is extensively employed across European measurement sites, particularly within the Cloudnet (Illingworth et al., 2007; Tukiainen et al., 2020) framework of the Aerosols, Clouds, and Trace Gases Research Infrastructure (ACTRIS). Renowned for its high sensitivity and reliability, MIRA-35's popularity is validated by various studies (Martucci and O'Dowd, 2011; Di Girolamo et al., 2012; Bühl et al., 2013; Griesche et al., 2020; Radenz et al., 2019). Görsdorf et al. (2015) offer comprehensive insights into the technical aspects of MIRA-35, accuracy considerations, and operational statistics based on over a decade of continuous measurements.

Unlike traditional MIRA-35 cloud radars operating in LDR-mode, which are commonly used for clutter filtering and detecting the melting layer, this paper employs the hybrid mode to study the ice crystal shape and orientation in detail. The hybrid mode, commonly used in weather radars (Ryzhkov et al., 2005), simultaneously transmits horizontal and vertical components of the signal, eliminating the need for expensive high-pulse-power polarization switching. Occasionally, this mode is also referred to as Simultaneous Transmission, Simultaneous Reception (STSR) mode. As demonstrated, the hybrid mode provides polarimetric parameters for a quantitative estimate of particle shape and orientation characteristics. In this paper the differential reflectivity (ZDR) and correlation coefficient (RHV), key parameters of polarimetric radar, are explored.

The observation by a polarimetric cloud radar is based on the capabilities of this radar type to detect the returned signals in two detection channels as function of Doppler velocity ω which are representative of the horizontally ($E_{\mathrm{h}}(\omega)$) and vertically ($E_{\mathrm{v}}(\omega)$) polarized planes of the received waves. Based on these two observables, polarimetric properties of the scatterers can be determined. Those are introduced in the following. It should be noted that detailed explanation of the calibration and calculation of polarimetric variables can be found in Myagkov et al. (2016a).

ZDR quantifies the difference between reflectivity measurements in horizontal (Z_{hh}, Eq. 1) and vertical (Z_{vv}, Eq. 2) polarizations, expressed in decibels (dB) (Eq. 3). $\langle\rangle$ denotes averaging over a series of pulses.

$$Z_{\mathrm{hh}}(\omega) = \left\langle \dot{E}_{\mathrm{h}}(\omega)\dot{E}_{\mathrm{h}}(\omega)^* \right\rangle \tag{1}$$

$$Z_{\mathrm{vv}}(\omega) = \left\langle \dot{E}_{\mathrm{v}}(\omega)\dot{E}_{\mathrm{v}}(\omega)^* \right\rangle \tag{2}$$

$$ZDR(\omega) = \frac{Z_{\mathrm{hh}}(\omega)}{Z_{\mathrm{vv}}(\omega)}. \tag{3}$$

At zenith-pointing direction, ZDR is zero. A positive ZDR value may indicate oblate-shaped ice particles, while a negative value may suggest prolate-shaped particles (Seliga and Bringi, 1976).

Atmospheric
Measurement
Techniques
Discussions
Open Access
EGU

The correlation coefficient (RHV) is a crucial parameter that quantifies the linear relationship between the Z_{hh} and Z_{vv}. Defined by Eq. 4, the correlation coefficient is defined by the ratio of the sums of the cross-polar elements and the square root of the product of the sums of the two co-polar elements and in the backscattering matrix.

$$RHV(\omega) = \frac{\left\langle \dot{E}_{\mathrm{h}}(\omega)\dot{E}_{\mathrm{v}}(\omega)^* \right\rangle}{\sqrt{\left\langle \dot{E}_{\mathrm{h}}(\omega)E_{\mathrm{h}}(\omega)^* \right\rangle \left\langle \dot{E}_{\mathrm{v}}(\omega)\dot{E}_{\mathrm{v}}(\omega)^* \right\rangle}} \tag{4}$$

Typically expressed as a value between 0 and 1. a correlation coefficient of 1 indicates perfect correlation or alignment between horizontal and vertical polarizations, suggesting consistent scattering behavior. Conversely, low values indicate a low correlation, associated with diverse or irregular scattering particles (Caylor et al., 1990). In polarimetric radar applications, this parameter is applied in the differentiation between precipitation types and in the identification of specific scattering mechanisms. For example, raindrops, with a spherical shape and uniform orientation, often exhibit higher correlation coefficients, while snow or hail particles, with irregular shapes and orientations, may result in lower correlation coefficients.

Linear Depolarization Ratio (LDR) is a parameter frequently detected by cloud radars which emit linearly polarized radiation only in one channel, but receive the co- and cross-polarized components of the backscattered signal. This kind of radar is usually referred to as LDR-mode cloud radar. The complex amplitudes of the received pulses in both the co-channel and cross-channel can be expressed as follows:

$$\dot{E}_{\mathrm{c}}(\omega) = E_{\mathrm{c}}(\omega)\exp(i\phi_{\mathrm{c}}(\omega)) \tag{5}$$

$$\dot{E}_{\mathrm{x}}(\omega) = E_{\mathrm{x}}(\omega)\exp(i\phi_{\mathrm{x}}(\omega)) \tag{6}$$

where E_{c}, ϕ_{c} and E_{x}, ϕ_{x} are amplitudes and phases of the received pulses in the co- and cross-channels, respectively. The LDR can be expressed as follows:

$$LDR(\omega) = \frac{\left\langle E_{\mathrm{x}}^2(\omega) \right\rangle}{\left\langle E_{\mathrm{c}}^2(\omega) \right\rangle} \tag{7}$$

It helps to characterize the nature and properties of scatterers within the radar beam. By examining how the backscattered power is distributed between both polarizations (horizontal and vertical), LDR aids in distinguishing different types of scatterers and understanding their orientation or shape within the radar pulse. LDR serves as a measure of randomness or isotropy in the scattering particles' orientation or shape in the plane perpendicular to the propagation direction of the radiation. Low LDR values imply a more ordered or isotropic scattering, often indicative of particles whose cross-sectional area appears isometric and well horizontally aligned with respect to the plane perpendicular to the propagation direction of the radiation (Trömel et al., 2021). LDR parameter contributes significantly to improving radar-based estimations of precipitation types, such as rain, snow, or hail, and enhances the accuracy of weather forecasts and observations.

3   Methodology

This section introduces the spectrally resolved shape and orientation retrieval. As the basis for this retrieval is the main-peak approach that was previously developed by Myagkov et al. (2016a), we will begin by outlining the principles of the established retrieval, followed by a detailed illustration of the spectrally resolved approach.

3.1   Main-peak approach

Melnikov and Straka (2013) illustrated that the shape of ice particles can be determined by exploitation of the elevation-angle dependency of polarimetric variables, an idea that is, e.g., utilized in the main-peak approach of Myagkov et al. (2016a) and the VDPS method of Teisseire et al. (2024) that is based on the latter. In the main-peak approach of Myagkov et al. (2016a), the fundamental concept involves the comprehensive analysis of ZDR and RHV across different elevation angles and at individual height levels. This analysis provides insights into particle habits by utilizing a spheroidal scattering model. The retrieval obtains a best fit between modeled and measured polarimetric parameters ZDR and RHV. In the modeling branch, simulations of ZDR and RHV are conducted for a comprehensive range of shapes, refractive index (particle density) and orientations of ice particles, spanning elevation angles from $30°$ to $150°$. In the observational branch, the analysis is concentrated solely on the main peaks of the signal-to-noise ratio (SNR) in all Doppler spectra observed over a range of elevation angles. The SNR is a measure used to quantify the level of a desired signal relative to the level of background noise. It is typically expressed as a ratio or in decibels (dB). The retrieval procedure then identifies the optimal match between the measured and modeled variables, utilizing this information to deduce the shape and orientation attributes of the ice particles. Myagkov et al. (2016a) employed the polarizability ratio ξ as a density-weighted axis ratio. This ratio ranges from 0.3 to 2.3. Within this range, values of $\xi = 0.3$ represent strongly oblate particles, $\xi = 2.3$ indicate strongly prolate particles, and $\xi = 1$ signifies centrally positioned spherical particles. As the polarizability ratio is also a function of the particle refractive index, i.e., density, its absolute value approaches unity for values of very low density. This aspect has to be considered in the interpretation of ξ. The retrieval also incorporates the degree of orientation κ, which indicates the spatial orientation of particles. The values of κ range from -1 to 1, where $\kappa = -1$ denotes a horizontal orientation for prolate particles and a vertical orientation for oblate particles. Conversely, a value of $\kappa = +1$ signifies a vertical orientation for prolate particles and a horizontal orientation for oblate particles. A value of 0 indicates randomly oriented particles.

3.2   Spectrally resolved approach

Ice particles adopt varying shapes, such as oblate, prolate or irregular, at the top of the cloud before descending based on their size. Along their descent, these particles interact by colliding either with other ice particles or with supercooled liquid droplets, or they grow by water vapour diffusion. The growth processes induce alterations in their shape, size, fall speed, and trajectory. Radar signals received from these particles can effectively discern their reflectivity and fall speed, when the radar is pointed vertically (e.g., to $90°$ elevation). Consequently, the Doppler spectra observed with a vertically pointing cloud radar offer insights into the variability of sizes and shapes of the ice particles. The width of the Doppler spectra is contingent upon

Atmospheric
Measurement
Techniques
Discussions

Open Access

EGU

the speed of different hydrometeor types and the dynamical structure of the cloud. Larger particles, characterized by higher fall speeds, contribute to broadening the Doppler spectra and to the eventual formation of distinct peaks in the Doppler spectrum (Radenz et al., 2019).

The approach of this study to advance the main-peak shape and orientation retrieval, referred to as the spectrally resolved approach, relies on the assumption that different hydrometeor types in a cloud volume are separated from each other by means of their different fall speeds, as was depicted in the previous paragraph. Figure 2 illustrates the block diagram of the spectrally resolved approach.

The spectrally-resolved shape and orientation retrieval is based on observations of the Doppler spectrum over a range of elevation angles. Primarily, the Doppler spectra observed at all elevation angles are divided into five parts (as illustrated in Fig. 1) for each of which the detected values of ZDR and RHV are used for independent application of the shape and orientation retrieval. While the conventional main-peak approach provides only one pair of ZDR and RHV, this approach yields five pairs for each Doppler spectrum over the range of elevation angles. Thereby, in principle any amount of spectral parts can be selected in the algorithm. The amount of 5 parts was empirically chosen for this study, because usually not more than that amount of different particle shapes can be expected in a cloud volume. Increasing the number of parts would result in a reduced amount of available data points per Doppler spectrum part which would lead to increased uncertainties. Note, that the different parts are not necessarily associated to individual peaks in the Doppler spectra, as they are e.g. derived by the peakTree method of Radenz et al. (2019). As will be outlined below, the observation of a cloud layer at different elevation angles makes it virtually impossible to track individual peaks in the Doppler spectra over the range of elevation angles. Instead, we assume that the fall attitude of the individual hydrometeor types contained in the cloud volume is similar at all elevation angles. E.g., the fastest-falling Doppler spectrum part at all elevation angles is associated to one hydrometeor type, and so on. Subsequent to the separation of the Doppler spectra at all elevation angles, the spectrally resolved approach operates akin to the main-peak approach, but for each spectral part separately. It compares the observed values of ZDR and RHV with their modeled counterparts for each data point. By identifying the best agreement, the approach retrieves the polarizability ratio and degree of orientation. Thus, five sets of values for polarizability ratio and degree of orientation are obtained for each height level, signifying to distinguish up to five distinct hydrometeor shapes and orientations.

In order to utilize the spectrally resolved approach, the Doppler spectra observed at the different elevation angles need to be harmonized as good as possible to derive the aforementioned estimate of the vertical-stare radial velocity for all angles. With increasing off-zenith angle, signatures of the falling particles get increasingly masked by contributions of the horizontal wind component. For the spectrally-resolved retrieval, it is thus aspired to obtain a best-estimate of the vertical component of the radial velocity at each elevation angle of the analysed RHI scans.

3.3 The influence of air motion on the Doppler spectra observed by a scanning cloud radar

The new spectrally resolved approach is based on the assumption of the ideal condition that the variability of the Doppler spectrum is caused by the differential fall motions of particles of distinct shape and orientation characteristics. Further, the signatures of the different shapes are required to be present homogeneously in the Doppler spectra from all elevation angles
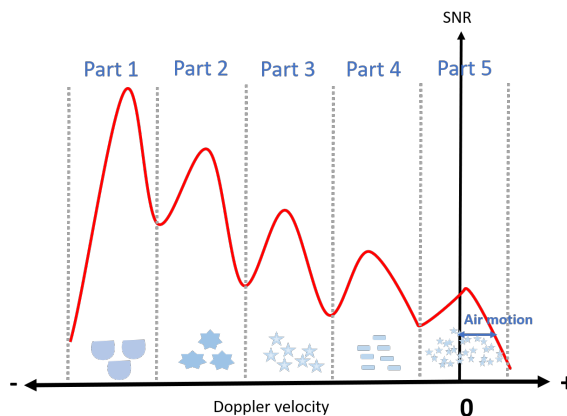
Figure 1. Partitioning the Doppler spectrum into five distinct parts.
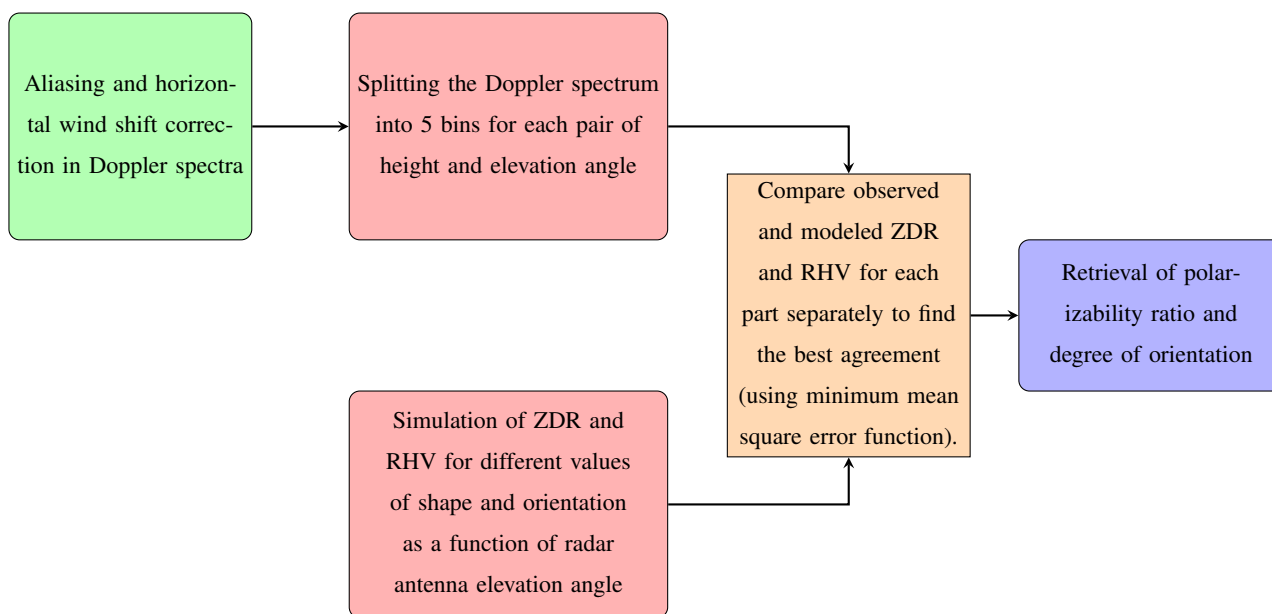

Figure 2. Block Diagram illustrating the Spectrally resolved approach.

220   probed by the cloud radar in the RHI scans of the shape retrieval, i.e., usually the range from 0 to $60°$ off-zenith angle
(30–$90°$ or 90–$150°$ elevation angle). In reality, atmospheric air motions occur, which introduce certain biases to the particle-
driven Doppler spectra at the different elevation angles. As depicted in Fig. 1 for a Doppler spectrum observed in zenith-
pointing direction, turbulent vertical motions are superimposed onto the gravitational downward motion of particles and result
in Doppler spectra which are broadened toward both positive and negative velocities. Horizontal winds also impact the Doppler
225   spectra, especially for lower elevation angles, by introducing a horizontal velocity component into the downward-pointing

component of the falling particles. Because the observation volume of a cloud radar is actually a conic section, a velocity wind shear within the radar observation volume introduces an artificial broadening of the Doppler spectrum, as well.

3.3.1 Retrieval of horizontal wind

In order to correct horizontal wind effects on the Doppler spectrum at different elevation angles, a best guess of the horizontal
230 wind vector is needed for each range gate to which the shape retrieval is about to be applied. A common approach to retrieve the profile of the horizontal wind with a scanning radar, is to employ a rotating beam that revolves around the vertical axis and focuses on a specific elevation angle to scan a circular area centered at the origin, which is commonly known as PPI (Plan Position Indicator) scan. Figure 3a visually represents the PPI scan geometry, showcasing the elevation angle ψ, azimuth angle β, wind speed vector V_{h}, wind direction angle α, and radial wind velocity V_{R}. This illustration provides a comprehensive
235 depiction of the various components involved in the PPI scan configuration. As the radar emits signals, it captures returns from particles scattered across the entire scanned circle. In this diagram, the wind direction is assumed to be westward. When the radar beam targets point A, the wind direction opposes the radar line of sight, resulting in the highest negative Doppler velocity. Conversely, when the radar beam aligns with point C, the wind moves parallel to the radar line of sight, yielding the highest positive Doppler velocity. At points B and D, where the radar line of sight is perpendicular to the wind direction, the Doppler
240 velocity registers at zero. Hence, the Doppler velocity acquired follows a sine pattern relative to the azimuth angle, termed the Velocity-Azimuth Display (Fig. 3b). The phase shift of the sine curve serves as an indicator for wind direction, while the sine curve's amplitude multiplied by the cosine of the elevation angle ψ yields the wind velocity (Eq.8). Additionally, the entire curve's displacement from the zero velocity signifies the precipitation fall speed. We used the approach of Baars et al. (2023) to derive the horizontal wind components.

245 $$V_{\mathrm{W}} = V_{\mathrm{h}} \cos(\beta - \alpha) \cos(\psi) \tag{8}$$
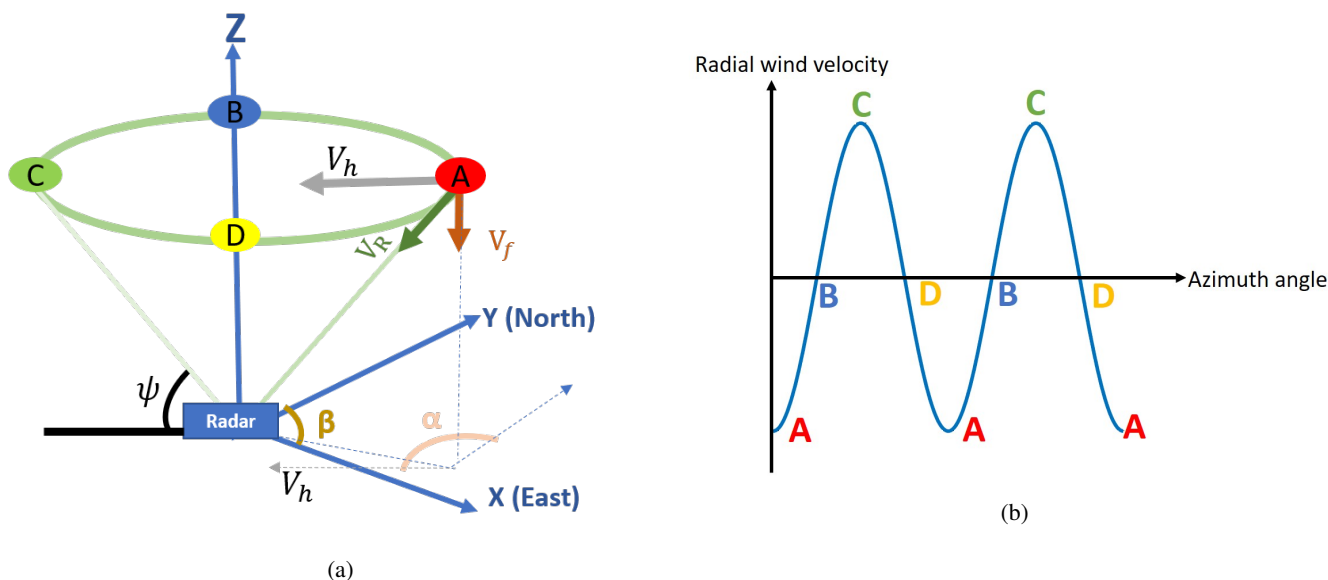
Figure 3. Representation of the horizontal wind vector by means of a PPI scan, showcasing the elevation angle ψ, azimuth angle β, wind speed vector V_h, wind direction angle α, and radial wind velocity V_R. (a) Illustration of the location of the 4 data points A, B, C, D which are orthogonal and perpendicular to the horizontal wind vector, respectively. (b) Angular relationship between horizontal wind vector and azimuth angle.

3.3.2 Aliasing problem and effects of horizontal winds on the determination of the vertical velocity component

Radars can ascertain particle speeds up to a limit known as the unambiguous (Nyquist) speed. Aliasing occurs when Doppler velocities surpass the Nyquist velocity. Especially at low elevation angles the contribution of the horizontal wind component can lead to Doppler velocities that surpass the Nyquist range. Additionally, the increasing contribution of the horizontal wind with decreasing elevation angle needs to be considered when the vertical component of the Doppler velocity, e.g., the best guess of the particle vertical velocity, is to be determined for all angles of an RHI scan. To address both the aliasing problem and the contamination of the vertical velocity component by the horizontal wind, the first step involves resolving any existing aliasing issues within the measured velocity. Subsequently, the correction for the horizontal wind effect in the determination of the vertical velocity component is carried out. These two corrections are detailed in the following subsections, each addressing their respective aspect.

1. Aliasing problem correction

Considering the characteristics of the Mira-35 cloud radar ($f_n = 5000\,\mathrm{s}^{-1}$, $\lambda = 8\,\mathrm{mm}$), the unambiguous speed for this radar v_{max} is $10.3\ \mathrm{m\,s}^{-1}$.

Folded velocities occur when Doppler velocities V_D surpass the Nyquist velocity v_max. The connection between the measured radial velocity V_R, Doppler velocity, and Nyquist velocity is defined by Equation 9:

$$V_\mathrm{R} = V_\mathrm{D} \pm 2nv_\mathrm{max} \tag{9}$$

Where n represents the Nyquist interval number as an integer. Correcting such folded velocities, often termed as unfolding or dealiasing, necessitates determining an appropriate value of n to retrieve the correct velocity. Various correction techniques, ranging from basic to sophisticated algorithms, have been proposed by researchers (Ray and Ziegler, 1977; Jing and Wiener, 1993). When Doppler velocity surpasses the v_max, the radar mistakenly deducts $2nv_\mathrm{max}$ from the true values. Conversely, when the Doppler velocity falls below $-v_\mathrm{max}$, the radar processing erroneously adds $2nv_\mathrm{max}$ to the true values, resulting in aliasing or folding issues. To address folding issues in the Doppler spectrum, the critical elevation angle, where the velocity matches the unambiguous velocity, for each specific height is determined. For elevation angles beyond this critical angle, Doppler spectra need to be shifted by $\pm 2nv_\mathrm{max}$. The correction involves a time-profile-by-time-profile examination (Johnson et al., 2020). It should be noted that if there is no aliasing problem, then $n = 0$, and consequently $V_\mathrm{R} = V_\mathrm{D}$.

2. Horizontal-wind correction

The velocities recorded in Doppler spectra often include contamination from radial wind velocity. To obtain a best guess of the downward-pointing velocity of hydrometeors, it is crucial to eliminate the radial wind speed component from the measured Doppler velocities. This process, known as horizontal wind correction, helps in retrieving a best guess of the true values of downward-pointing component of the velocity vector at all elevation angles and thus the falling attitude of the observed cloud hydrometeors. By subtracting the radial wind speed (Equation 8) from the aliasing-corrected radial particle's speed, one can derive corrected values for the particles' radial speed $V_\mathrm{R,cor}$ (Eq. 10).

$$V_\mathrm{R,cor} = V_\mathrm{R} - V_\mathrm{W} \tag{10}$$

4 Application and results

The strength of the main-peak approach to derive the shape and orientation of hydrometeors formed in supercooled stratiform clouds was effectively proven by Myagkov et al. (2016a, b) and produced valuable results due to the homogeneity of this cloud type. In contrast, deep clouds comprise a variety of hydrometeor types, limiting the main-peak approach to identify only the dominating one, while others remain undetected. In this section, an application of the spectrally resolved approach will be presented by means of different case studies. The novelty of the presented method will be highlighted by comparing the results to the results obtained from the main-peak approach.

Atmospheric
Measurement
Techniques
Discussions

Open Access

EGU

4.1 First case study 07 Nov 2014, 09:15 – 09:30: retrieval of various hydrometeor types

A deep cloud system that was observed on November 7, 2014, during the period from 09:15 to 10:00 UTC, in Cabauw, the Netherlands, is illustrated in Fig. 4 (Hajipour et al., 2024). Figure 4, is divided into six panels. Panels a, b, c, and d depict the radar reflectivity, LDR, Doppler velocity, and spectral width respectively, recorded by the vertically pointed Mira-35 NMRA

290   radar. Additionally, panels e and f showcase the attenuated backscatter coefficient at 1064 nm and volume depolarization ratio at 532 nm measured by the PollyXT lidar. The deep cloud that was present during the period from 09:15 to 09:30 UTC serves as the case study.
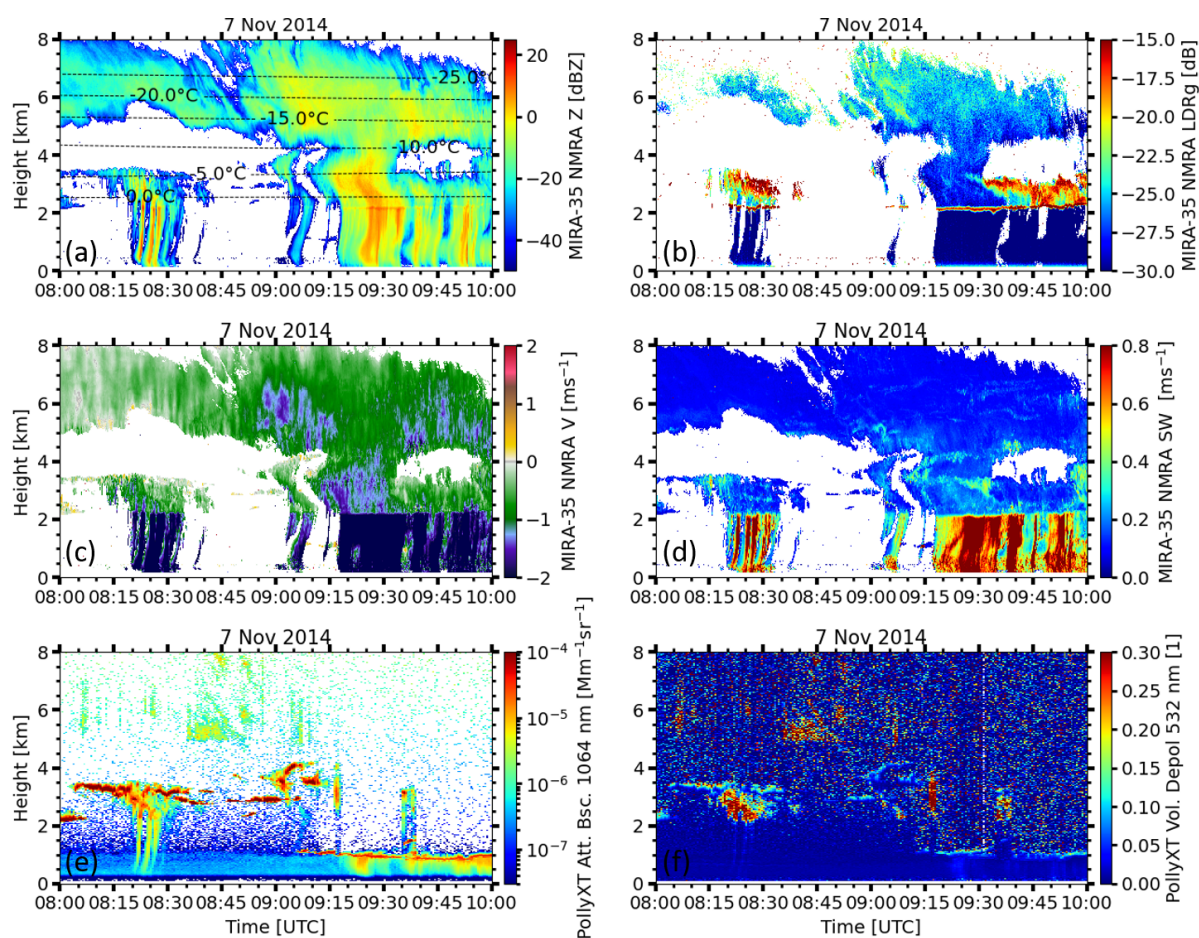
Figure 4. (a) Radar reflectivity, (b) LDR, (c) Doppler velocity, (d) spectral width measured by Mira-35 NMRA and (e) attenuated backscattered coefficient, and (f) volume depolarization ratio measured by PollyXT lidar as observed on November 3, 2014. The time interval from 09:15–09:30 UTC and altitude range from 0–8000 m correspond to the case study to which the main-peak shape retrieval method was applied (see Fig. 5). Similarly, the time interval from 09:45–10:00 UTC and altitude range from 0–4000 m correspond to the case study to which the spectral shape retrieval method was employed (see Figs. 6) – 8.

Between 09:15 and 09:30 UTC, a deep cloud, reaching up to 8 km height was present above Cabauw, which caused precipitation after 09 UTC. Ice particles descended, creating a melting layer at approximately 2 km altitude. The evolution of the

295   mixed-phase in this deep cloud spanned from the melting layer up to its top at around 8 km altitude during the specified time period. At cloud top, the LDR was approximately -25 dB and decreased to around -30 dB close to the melting layer. To assess the morphology of the dominating ice particle population in this cloud, the main-peak approach was applied first.

Figure 5 demonstrates the quantification of the parameters relevant for the retrieval of the ice particle shape and orientation by means of the main-peak approach. The polarizability ratio at cloud top is 0.79 and shows a slight increase with decreasing

300   height (0.83 at 5 km height), indicating the presence of rather isometric or slightly oblate particles. Descending to an altitude of 4 km, the determined polarizability ratio remains approximately 1.1, suggesting the continued existence of a spherical shape with a tendency of slight prolateness. Afterward the polarizability ratio gradually decreases to almost 1 at a height of 2.3 km, suggesting a transition toward strong spherical particles.

As shown in Fig. 4, two distinct thin clouds at varying altitudes are observable during the 9:30 to 10:00 UTC period. Precip-

305   itation from the upper-level cloud layer with a top height of 7 km stops, revealing a lower-level cloud layer with a top height of about 3.5 km. This layer exhibits depolarization signatures (as depicted in Fig. 4 b), indicating a shift in the shape of ice particles towards non-spherical. In the deep cloud (09:15 to 09:30 UTC) discussed above, no evidence of depolarization was observed in the moment data at the same altitude range ($2.3 - 3$ km), suggesting the presence of isometric particles as it was also confirmed by application of the main-peak shape and orientation retrieval.

310   As result of a next analysis step, Figures 5 c, and d illustrate the analysis of polarizability ratio and degree of orientation as quantified by the main-peak approach for the thin cloud layer for an RHI scan performed from 09:46 and 09:48 UTC. The derived polarizability ratio and degree of orientation for the layer between 2 and 3 km height clearly show the presence of predominantly horizontally aligned prolate ice crystals.
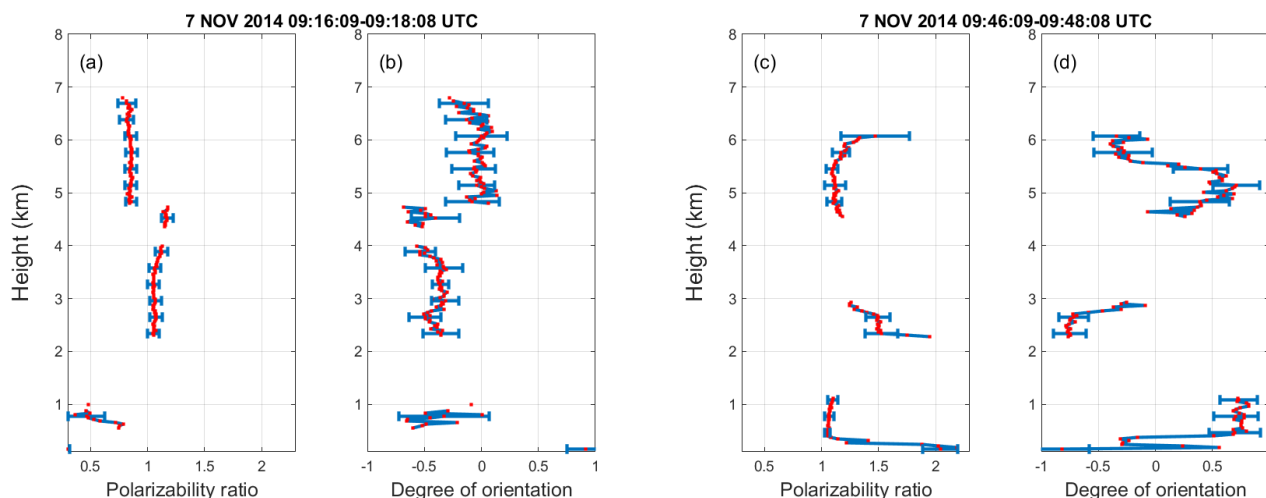
Atmospheric
Measurement
Techniques
Discussions
Open Access
EGU

Figure 5. (a) Polarizability ratio and (b) degree of orientation values retrieved by the main peak approach from a Mira-35 RHI scan performed at 09:16--09:18 UTC, and (c) Polarizability ratio and (d) degree of orientation values retrieved by the main peak approach from a Mira-35 RHI scan performed at 09:46–09:48 UTC on November 7, 2014.

In summary, the main-peak approach effectively identifies the primary hydrometeor types in the deep cloud (spherical particles) and the thin cloud (prolate particles). The occurrence of prolate-shaped particles in the thin cloud shortly after the formation of the deep cloud suggests the possible coexistence of prolate-shaped particles within the deep cloud at heights ranging from 2.3 to 3 km, although they may not be the prevailing particle morphology. Due to notable changes within the cloud from 9:30 to 9:45 UTC, the dominant particle shape transitions from spherical to prolate, and this transition is captured by the main-peak approach during the 9:45 to 10:00 UTC period. Consequently, the main peak approach may not accurately identify this particular hydrometeor type in the deep cloud.

Figure 6 presents height-vs-distance cross-sections showing the SNR, ZDR, and RHV across the five selected parts of the Doppler spectra obtained during an RHI scan that was performed from 09:16–09:18 UTC. This visual representation offers an insightful view of these parameters across different parts of the Doppler spectra acquired within the specified time frame and over the range of elevation angles covered by the RHI scan.

The spectrally resolved approach starts with splitting the Doppler spectra at all individual height levels with a vertical resolution of 30 m. Splitting the spectra into the 5 parts allows a separate analysis of different particle types which might be present in the probed cloud volume. In Fig. 6 a and e, SNR in parts 1 and 5 appears lower compared to other parts, indicating possible contamination of ZDR and RHV data by noise. Dealing with noise is an inherent challenge in the spectrally resolved approach, particularly noticeable in the first and last Doppler parts. Figure 6 a reveals low SNR levels above 4 km height, with most data points above 6 km height registering below 20 dB. This diminished SNR at higher altitudes fails to reflect clearly in ZDR and RHV profiles of part 1 of the Doppler spectra, representing the fastest falling particles. In Fig. 6 f, between heights of $5.2 - 6.1$ km, the ZDR profile around the vertical angle hovers near 0 dB. With a decrease in elevation angle, ZDR slightly

increases to approximately $0.5\,\text{dB}$, resembling the main peak of ZDR. Correspondingly, RHV at these heights consistently remains close to 1. These ZDR and RHV signatures suggest the presence of oblate-shaped particles in these altitudes. At heights ranging from the melting layer ($2.3\,\text{km}$) to $4\,\text{km}$, the SNR stabilizes at approximately $60\,\text{dB}$. ZDR variations with decreasing elevation are less pronounced at these heights, while RHV remains close to 1. These characteristics suggest the presence of oblate-shaped particles within this height range. Figure 6 b displays relatively high SNR for part 2 of the analyzed Doppler spectra, implying less noise contamination compared to part 1. However, at certain altitudes between $3.9 - 5.6\,\text{km}$, low SNR levels hinder discernible signatures in ZDR and RHV profiles, making their retrieval challenging. Conversely, at heights where SNR is high within this range, RHV remains close to 1, indicating a lack of significant variations. In Figure 6 c, higher SNR values provide clearer ZDR and RHV signatures for part 3, as shown in Fig. 6 h and m. Across both higher and lower cloud layers, ZDR shows a slight increase with decreasing elevation angle, while RHV remains consistently close to 1, indicative of oblate-shaped particles in this section. Figures 6 d, i, and n, representing part 4, exhibit signatures consistent with oblate-shaped particles observed at various heights. However, in Figures 6 j and o (part 5), insufficient valid data above $4\,\text{km}$ is evident, and different particle signatures are observable below $4\,\text{km}$. Below $4\,\text{km}$, RHV at the zenith angle registers at its
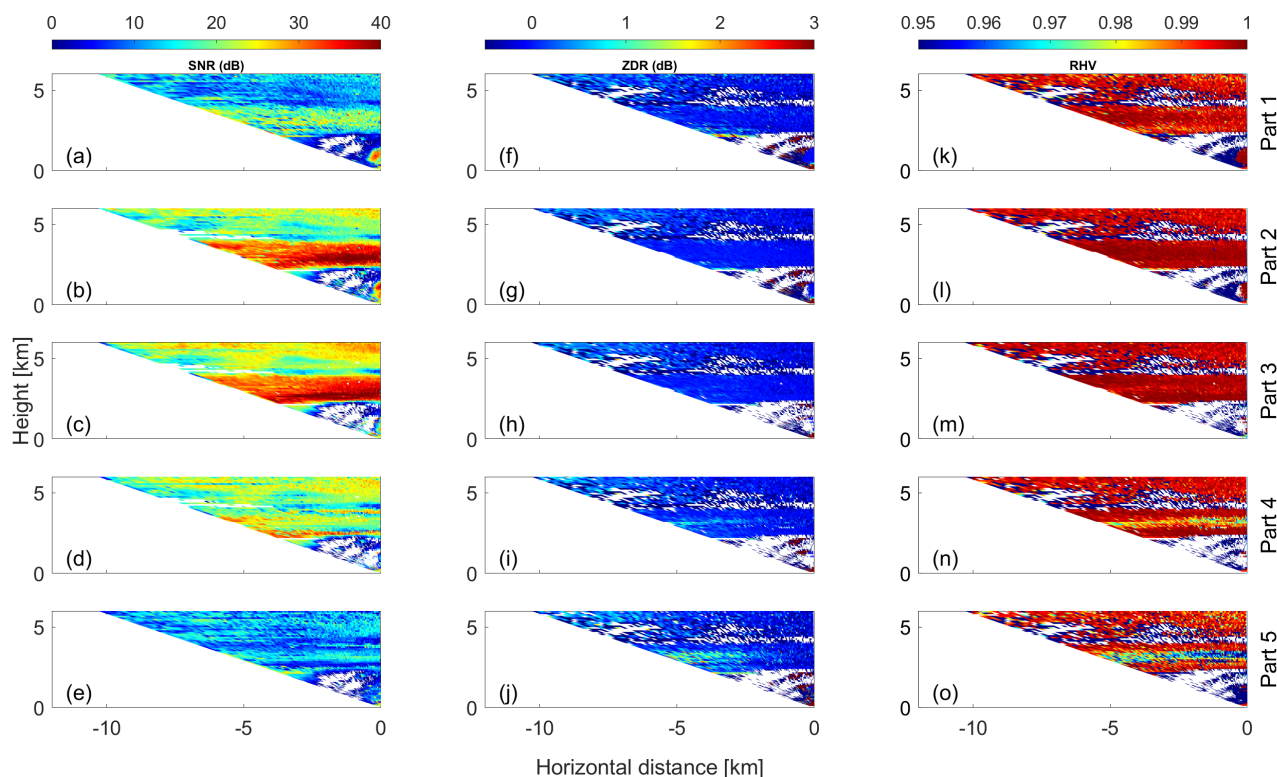

Figure 6. Height-vs-distance cross-sections of: (a) SNR, (f) ZDR, and (k) RHV in part 1, (b) SNR, (g) ZDR, and (i) RHV in part 2, (c) SNR, (h) ZDR, and (m) RHV in part 3, (d) SNR, (f) ZDR, and (n) RHV in part 4, (e) SNR, (j) ZDR, and (o) RHV in part 5 of the Doppler spectrum as derived from a RHI scan of Mira-35 MBR4 performed at Cabauw, NL, on November 7, 2014, 09:16–09:18 UTC.

Atmospheric
Measurement
Techniques
Discussions

Open Access
EGU

lowest value around 0.96, increasing with decreasing elevation angle. ZDR also exhibits an increase with decreasing elevation angle at these heights, suggesting the presence of prolate particles in part 5 which is representing the slowest-falling particles.

Since different parts might identify oblate-shaped particles at heights around $3\,\mathrm{km}$ (parts 1, 2, 3, and 4) and prolate-shape particles at part 5, a height of $3\,\mathrm{km}$ is chosen for a detailed depiction of the data analysis procedure. Figures 7 a and g showcase

350 complete Doppler spectra of ZDR and RHV at the height of $3.1\,\mathrm{km}$. Figures 7 -b–f and h–l show the elevation dependency of ZDR and RHV for each of the 5 spectral parts, respectively. In general, homogeneity in ZDR and RHV as a function of elevation angle is given for parts 1 (fastest falling part) to 3, but notable differences are indicated for parts 4 and 5, corresponding to the slow falling particles. These discrepancies are more discernible at higher off-zenith angles, emphasizing the elevation-dependent nature of ZDR and RHV. Figure 7 demonstrates well that splitting the spectra into 5 parts allows for separate

355 analysis of different particles, as will be demonstrated in more detail in the following.

In Figs. 7 -b to d, the ZDR values remain homogeneous across all elevation angles, centered around $0\,\mathrm{dB}$. Similarly, in Fig 7 h to j, the RHV values exhibit uniformity across elevation angles, consistently equal to 1. These ZDR and RHV signatures collectively suggest the presence of spherical-shaped particles in parts 1 to 3. In Fig. 7 -e, and f the ZDR values at low elevation angles surpass those at the zenith angle. Additionally, in Fig. 7 -k, and l RHV at zenith pointing direction is at its minimum

360 and shows a slight increase toward lower elevation angles. These signatures suggest the potential presence of prolate-shaped particles.
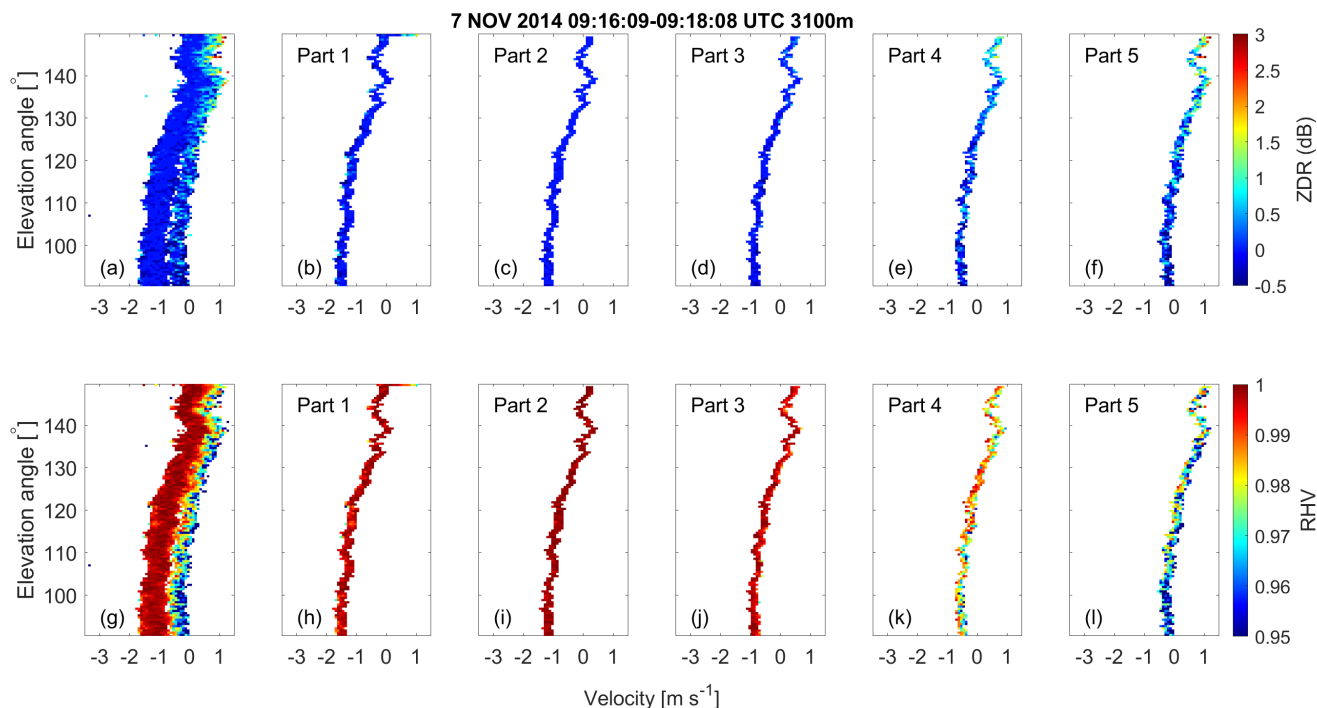
Atmospheric
Measurement
Techniques
Discussions

Figure 7. Doppler spectra of ZDR and RHV as a function of elevation angle and for each part of the spectrally resolved shape and orientation retrieval as obtained for 3.1 km height on November 7, 2014, at 09:15:09 UTC. (a) ZDR spectrum before segmentation, (b) to (f): ZDR spectrum in parts 1 to 5 after splitting, (h) RHV spectrum before splitting, (h) to (l): RHV spectrum in parts 1 to 5 after splitting.

Figure 8 illustrates the retrieved profiles of polarizability ratio and degree of orientation obtained through the spectrally resolved approach. For the sake of readability, error bars are omitted in this case, as they are in the same order of magnitude as the ones shown in Fig. 5 for the main-peak approach. At an altitude of approximately 6 km, the retrieved polarizability

365 ratio for parts 1 and 2 is 0.9 and 1.1, respectively. This indicates that spherical particles dominate from the cloud top down to an estimated height of 5.5 km. However, there's a data gap between 5.5 and about 4 km height, caused by the too-low SNR values and general lack of data points in this height range. Between a height close to 4 km and down to 2.5 km, the analysis identifies the coexistence of two distinct hydrometeor types. Spherical particles are retrieved from parts 1 (fastest falling part) to 4, indicating their prevalence, while part 5 (slowest falling part) reveals the existence of prolate particles. The

370 prolate shape becomes more evident as height decreases from around 4 km, with the most pronounced prolate shape observed at approximately 3 km, boasting the highest polarizability ratio of around 1.7. As the height decreases further towards the melting layer (height of 2.5 km), the prolate particles transition into a more spherical shape.

Based on the presented analysis and the detected co-location of rather spherical particles and prolate particles in the lower part of the cloud system between 09:15 and 09:30 UTC (Fig. 4), relevant conclusions can be drawn. The detected prolate

375 particles were most-likely formed in-situ in the lower layer. Seeding by the upper layer does not seem to have any effects, since

prolate ice crystals are also present when no seeding occurred from above (after 09:30 UTC in Fig. 4). This case thus highlights that the simultaneous presence of particles from a seeder cloud and prolate particles does not necessarily mean that secondary ice formation was triggered by the seeding of particles from higher altitudes into the lower-level cloud layer.
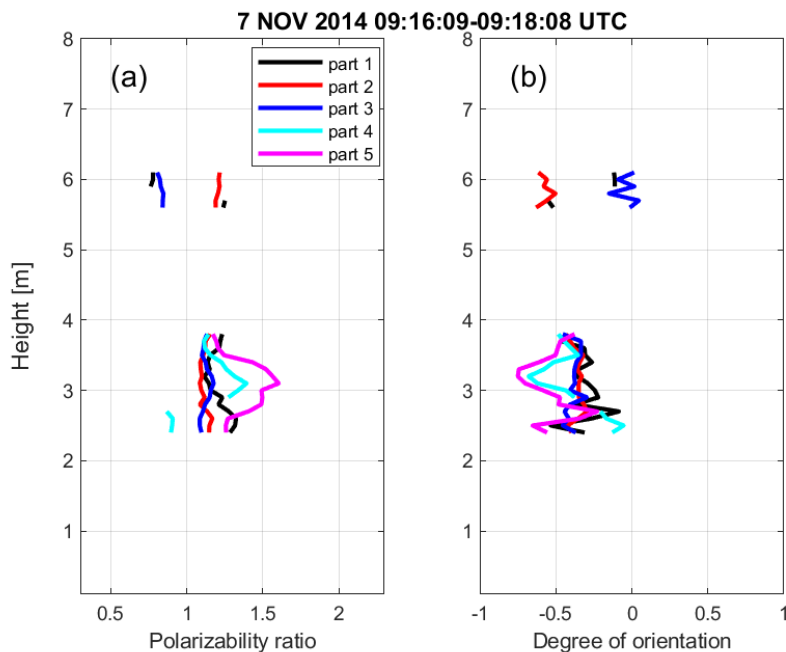

Figure 8. (a) Vertical profiles of polarizability ratio and (b) degree of orientation retrieved by the spectrally resolved approach for a RHI scan of Mira-35 MBR4 performed at Cabauw, NL, on November 7, 2014, 09:16–09:18 UTC.

4.2 Second case study 03 Nov 2014, 20:30 – 20:45: Secondary ice formation

380 The objective of this section is to illustrate how the introduced spectrally resolved approach, in combination with Mira-35 NMRA, can unveil secondary ice production. Based on a secondary ice retrieval from zenith-pointing LDR-mode cloud radar observations, Li and Moisseev (2020) demonstrated a unique phenomenon: the emergence of a two-layer LDR signature within a singular melting layer. Through thorough analysis of Doppler spectra observations, it was revealed that the upper LDR layer results from the melting of ice needles, possibly formed through the rime-splintering process, whereas the lower layer primarily

385 arises from the melting of background ice particles originating at the cloud top. Additionally, above the two-layer LDR region, an area characterized by relatively high LDR values was observed, suggesting that such elevated LDR values in ice may be ascribed to prolate needle-like particles. Prolate-shaped particles situated above the melting layer, being smaller than other hydrometeor types, descend at a slower rate compared to their larger counterparts, covering a shorter distance within a given timeframe. Consequently, this phenomenon was identified to give rise to the observation of two distinct layers of LDR. Using 2

390 years of vertical-stare polarimetric cloud radar observations, Li et al. (2021) derived a statistics of the occurrence of columnar

ice crystals in co-location to the presence of other cloud hydrometeor types, such as aggregates, graupel or pristine crystals of shapes different to the columnar one. They used these statistics to estimate the intensity of secondary ice formation and eventually derived an ice multiplication factor by comparing the derived secondary ice crystal concentrations to estimates of the concentration of ice nucleating particles. While the studies of Li and Moisseev (2020) and Li et al. (2021) highlight the

395 applicability of vertical-stare cloud radar measurements for identification of columnar ice (presumably secondary ice) within a population of otherwise non-depolarizing ice crystals, their method is not able to infer any specific information about the background population of ice crystals from which the secondary ice formed. Reason is, that oblate and isometric/spherical particles feature similar LDR signatures when observed with a zenith-pointing cloud radar. In the following within this section, the applicability of the spectrally resolved shape and orientation retrieval to identify both, the shape and orientation of the

400 background and of the secondary ice populations, will be presented.

The case study of secondary ice formation in a deep cloud system over Cabauw was conducted for the time interval from 20:37 to 20:47 UTC of 3 November 2014 (Hajipour et al., 2024). In Figure 9, panels a, b, c, and d, showcase time-height cross-sections of radar reflectivity factor, LDR, Doppler velocity, and spectral width measured by the zenith-pointing Mira-35 NMRA. Panels e and f display time-height cross-sections of attenuated backscatter coefficient at 1064 nm and volume

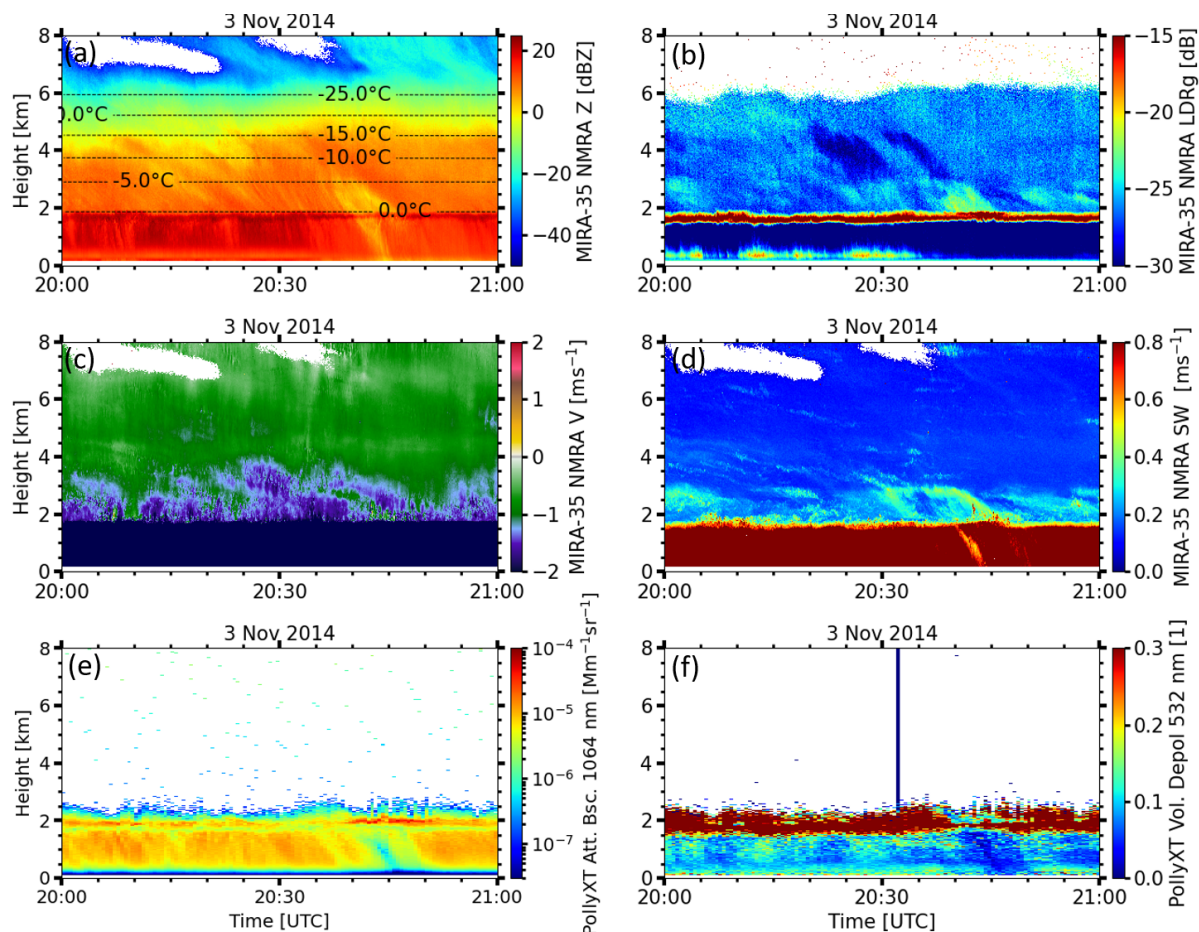405 depolarization ratio at 532 nm recorded by the PollyXT lidar.

Figure 9. (a) Radar reflectivity, (b) LDR, (c) Doppler velocity, (d) spectral width measured by the Mira-35 NMRA. (e) Attenuated backscattered coefficient, and (f) the volume depolarization ratio measured by Polly XT lidar on November 3, 2014, during the time window 20:00 to 21:00 UTC in Cabauw. The highlighted period (20:37–20:47 UTC) and altitude range (0–8000 m) signify the focus of the case study where shape retrievals are applied.

Within this case study, LDR values around $-25\,\mathrm{dB}$ at the cloud top as observed by vertical-stare Mira-35 NMRA indicate the presence of slightly non-isometric-shaped particles. Figure 10 a, and b present the profiles of polarizability ratio and degree of orientation, respectively, as obtained using the main-peak approach across four consecutive RHI scans of Mira-35 MBR4 that were performed between 20:01 and 20:11 UTC. In all RHI scans, the polarizability ratio at the cloud top registers at 0.8, indicating the prevalence of predominantly isometric or slightly oblate particles. Progressing from the cloud top to the height of 4.5 km, a slight increase in the polarizability ratio is observed in the second RHI scan, reaching 0.9, indicative of particles with an isometric shape. At 2 km height, the melting layer can be identified by the presence of very low polarizability ratios and a random degree of orientation of approximately 0. Below the melting layer, the presence of spherical rain droplets is indicated.
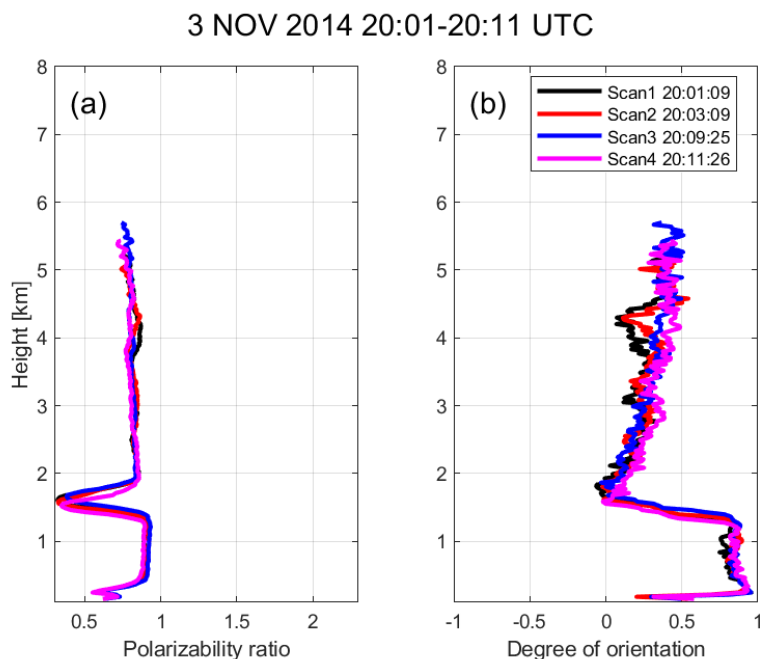
Figure 10. (a) Polarizability ratio and (b) degree of orientation values retrieved by the main-peak approach from 4 RHI scans of Mira-35 MBR4 performed at Cabauw, NL, on November 3, 2014, 20:01:09-20:11:26 UTC.

Figure 11 provides a closer examination of the LDR profiles observed between 20:30 and 21:00 UTC, revealing the presence
415   of a secondary layer of elevated LDR values at altitudes between the melting layer and 2.75 km height during the period from
20:40 to 20:47 UTC. As Li et al. (2021) demonstrated, secondary ice production can be identified by analyzing LDR spectra
obtained from a vertically pointed cloud radar, such as Mira-35 NMRA. This approach will be evaluated in the following.
Figures 12a and b, akin to Figure 3a and b of Li et al. (2021), illustrate profiles of radar reflectivity and LDR spectra acquired
from Mira-35 NMRA for the 10-s time period ending at 20:41:37 UTC. Elevated radar reflectivity levels detected at an altitude
420   of 2.9 km within the lower velocity range of the Doppler spectrum suggest the existence of various hydrometeor types. Further-
more, a significant increase in LDR values up to around -17 dB was observed from the altitude above the melting layer up to
the height of 2.9 km in the slow-falling velocity range of the Doppler spectrum, implying the predominance of prolate-shaped
ice particles in this part of the Doppler spectrum. To delve deeper into the analysis and retrieve hydrometeor types also from
the fast-falling mode with more detail, the spectrally resolved shape and orientation approach was applied specifically to the
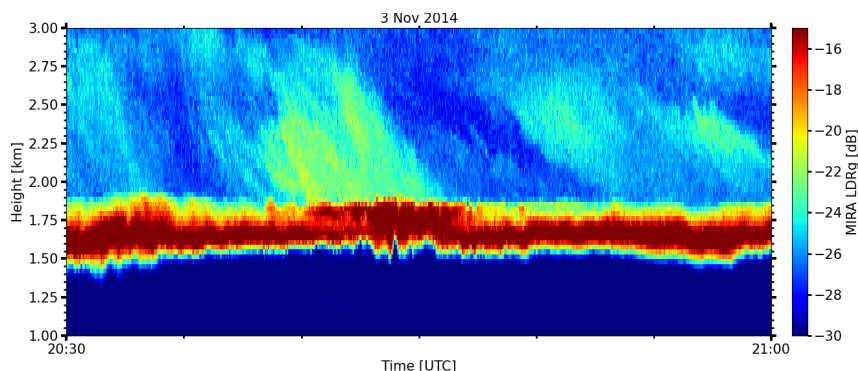425   RHI scan recorded during the period from 20:41:27 to 20:43:24 UTC.

Figure 11. Time-height cross section of LDR observed by Mira-35 NMRA during the time interval from 20:30 to 21:00 UTC on 3 November, 2014, in Cabauw, the Netherlands. Elevated LDR signatures were detected at altitudes from above the melting layer and 2.75 km height during the time period from 20:40-20:47 UTC.
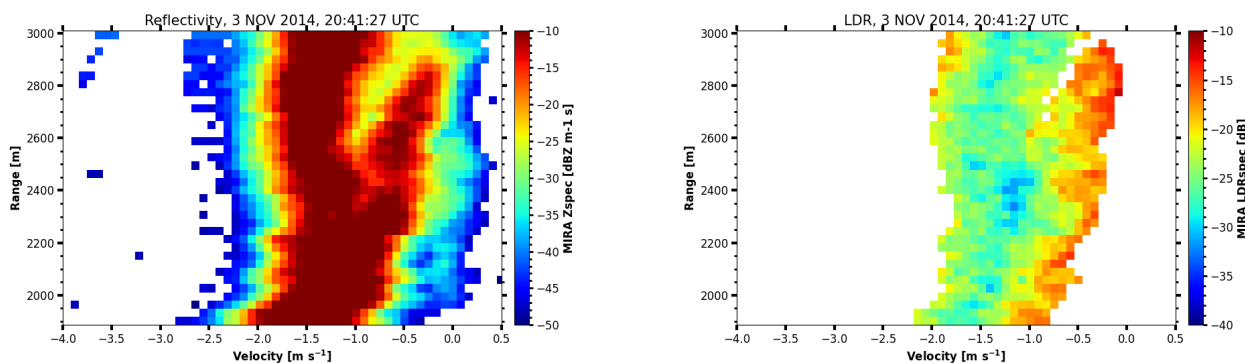

Figure 12. Profiles of Doppler spectra of (a) radar reflectivity and (b) LDR at 20:41:27 UTC, on 3 November 2014 measured by Mira-35 NMRA in Cabauw, the Netherlands.

Figure 13 presents height-vs-distance cross-sections displaying SNR, ZDR, and RHV for parts 1 (fastest falling) to 5 (slowest falling) extracted from the selected RHI scan. For parts 1 to 4, the signatures of ZDR are rather similar at all heights above the melting layer (i.e., above 2 km height). Only in the cloud-top region between 4 and 5 km height, the gradient of ZDR vs. elevation is increasing from parts 1 to 4. RHV shows enhanced fluctuations between the different spectral parts 1 to 4. Part 1 features rather noisy RHV signatures at all heights and elevation angles, which are on average slightly below 1. For parts 2 to 4, RHV is approximately constant at all elevation angles at heights above 3 km. At heights below 3 km and above the melting layer, RHV decreases with decreasing part number (i.e., with slower-falling Doppler velocities). Both, ZDR and RHV of part 5 show some deviations from the general behavior of the other parts. First, at all heights, ZDR increases with increasing off-zenith angle. Second, RHV from between the melting layer and about 4 km height is constantly low for all elevation angles. When interpreting the reported signatures of ZDR and RHV, SNR should be considered, as well. In regions of the cloud layer

where SNR was below 20 dB, noise artifacts could lead to a reduction of the average values and an increase of variability of RHV. This can potentially be an issue for heights above 3 km of part 1 or for some height regions around 4 km of part 5.
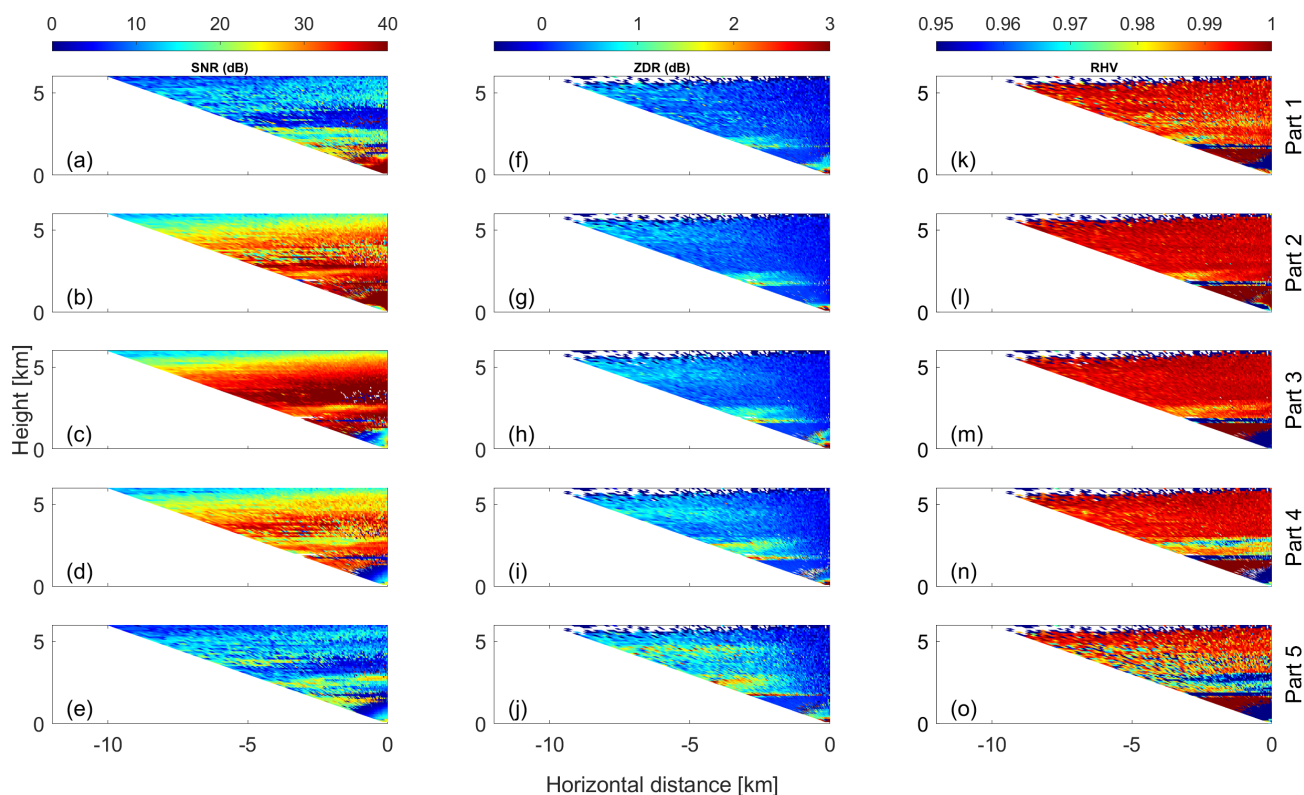

Figure 13. Height-vs-distance cross-sections of: (a) SNR, (f) ZDR, and (k) RHV in part 1, (b) SNR, (g) ZDR, and (i) RHV in part 2, (c) SNR, (h) ZDR, and (m) RHV in part 3, (d) SNR, (f) ZDR, and (n) RHV in part 4, (e) SNR, (j) ZDR, and (o) RHV in part 5 of the Doppler spectrum as derived from a RHI scan of Mira-35 MBR4 performed at Cabauw, NL, on November 3, 2014, 20:41–20:43 UTC.

What remains despite the low-SNR regions that occurred at some heights and spectral parts of the case study, is the general feature in ZDR and RHV within the first km above the melting layer. Exemplary for this region, the velocity-vs-elevation displays for the polarimetric parameters for the height level of 2200 m are shown in Fig. 14.
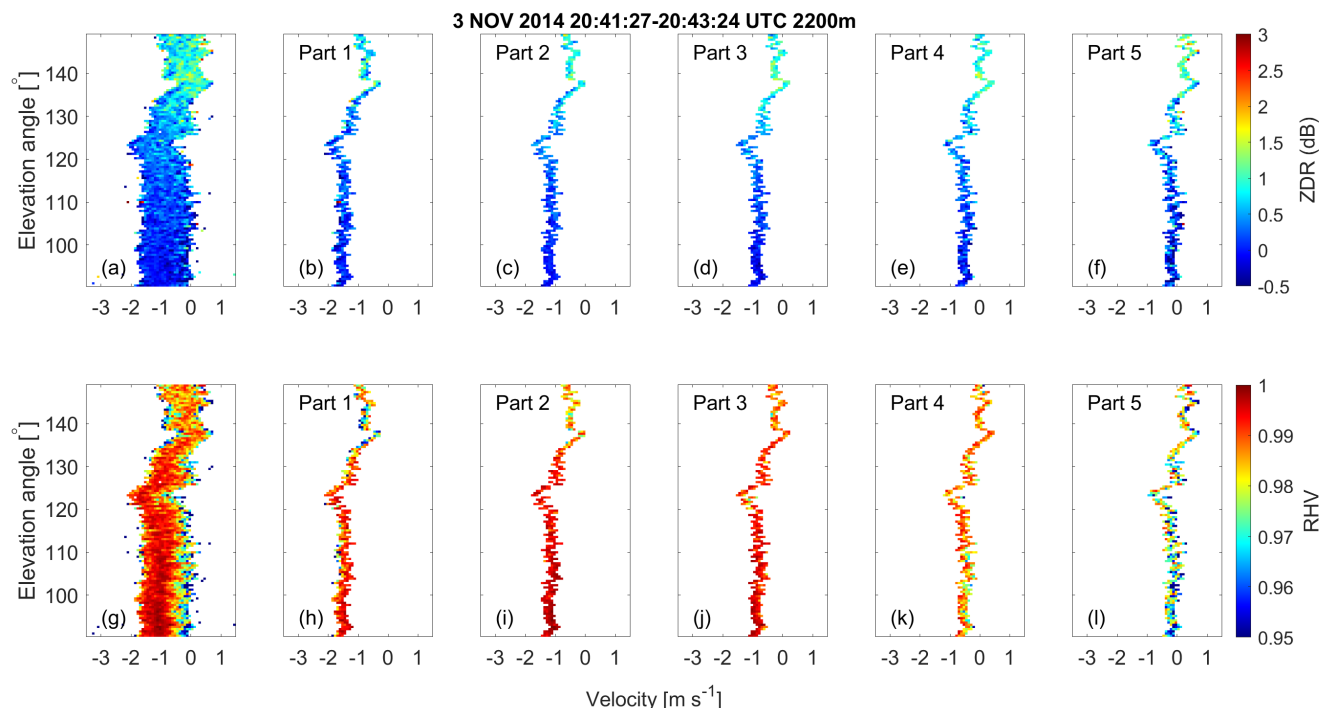
Figure 14. Doppler spectra of ZDR and RHV as a function of elevation angle and for each part of the spectrally resolved shape and orientation retrieval as obtained at 2.2 km height. (a) ZDR spectrum before splitting, (b) to (f): ZDR spectrum in parts 1 to 5 after splitting, (h) RHV spectrum before splitting, (h) to (l): RHV spectrum in parts 1 to 5 after splitting.

Representative for the height levels above 2.5 km, Fig. 15 provides similar illustrations for the height level of 3200 m. By comparing the layers of 2200 and 3200 m, the increased elevation dependency of ZDR and RHV at 2200 m height becomes visible. At 2200 m height, most parts feature oblate-like signatures which are stronger than the ones at 3200 m height. In addition, due to the reverted elevation dependency of RHV in combination with the general elevation dependency of ZDR, part 5 at 2200 m height is indicative of prolate particles.
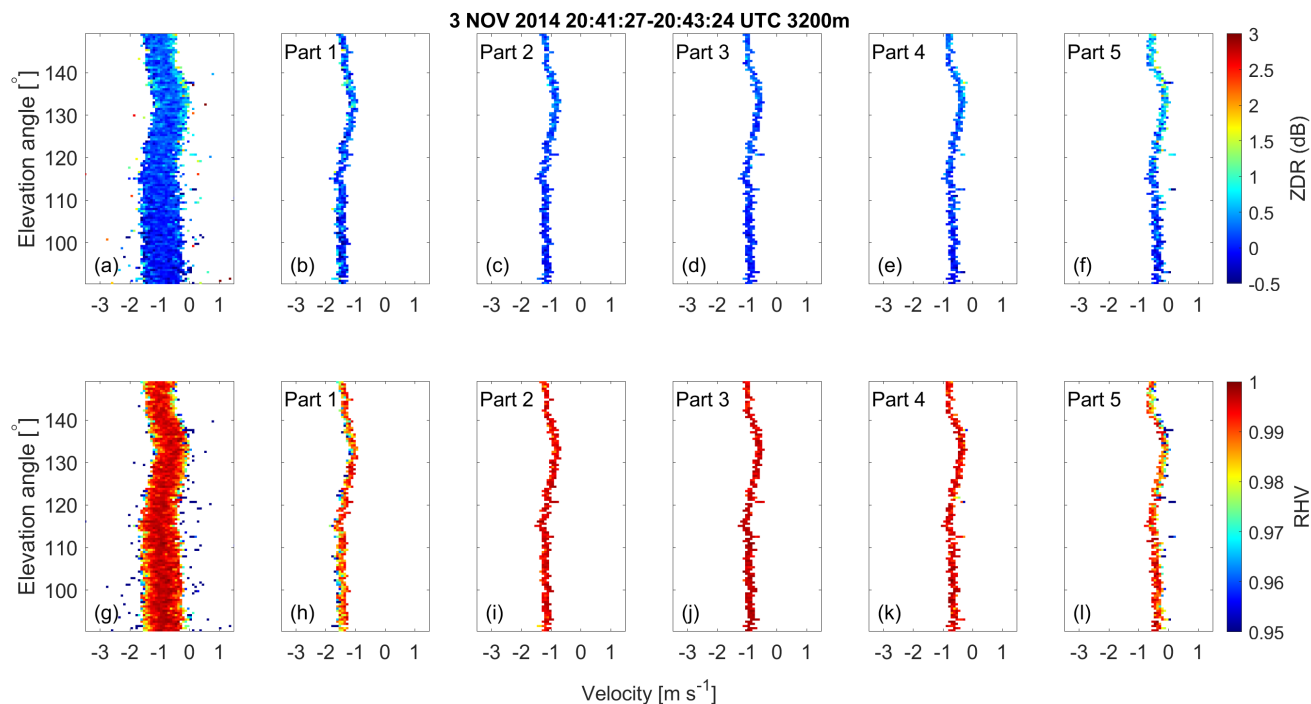
445

Atmospheric
Measurement
Techniques
Discussions

Open Access

Figure 15. Doppler spectra of ZDR and RHV as a function of elevation angle and for each part of the spectrally resolved shape and orientation retrieval as obtained at 3.2 km height. (a) ZDR spectrum before splitting, (b) to (f): ZDR spectrum in parts 1 to 5 after splitting, (h) RHV spectrum before splitting, (h) to (l): RHV spectrum in parts 1 to 5 after splitting.

Quantitatively, this contrast in particle shape structure is illustrated in Fig. 16, which portrays the derived profiles of the polarizability ratio and degree of orientation obtained using the spectrally resolved approach. Parts 2, 3, and 4 reveal the presence of slightly oblate-shaped particles, with part 4 indicating a more pronounced oblate shape at heights below 3 km and the melting layer, compared to parts 2 and 3. In part 1, the retrieval process tends toward the identification of ice particles with shapes closely resembling spheres, which tend to exhibit oblate characteristics. In part 5, the retrieval method distinguishes prolate-shaped particles above the melting layer and below an altitude of 3 km. Simultaneously, it identifies oblate-shaped particles at altitudes exceeding 3 km.
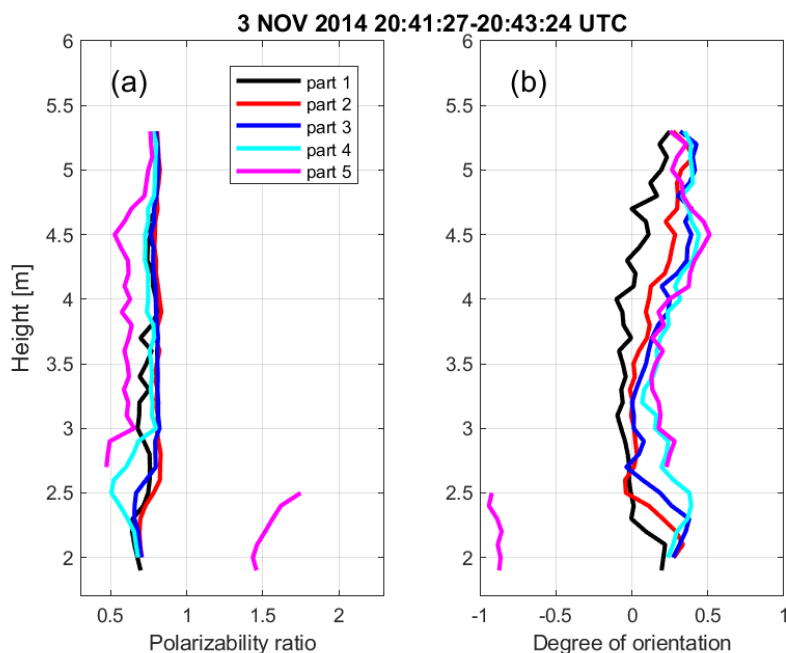
450

Figure 16. (a) Polarizability ratio and (b) degree of orientation values retrieved by spectrally resolved approach from a RHI scan of Mira-35 MBR4 at 20:41–20:43 UTC performed at Cabauw, NL, on November 3, 2014.

In conclusion, the spectrally resolved approach demonstrates the coexistence of various particle types, possibly different in size, within this case study. Additionally, it suggests the possibility of secondary ice formation. In contrast, the original main-peak approach, focusing on the strongest SNR, suggests the presence of only isometric particles. Based on the presented case study of secondary ice formation it is also obvious that the spectrally resolved shape retrieval provides information about the particle shape distribution that is superior to the information content that can be obtained from zenith-pointing LDR-mode cloud radar observations. Vertical-stare observations are well suited to identify secondary, prolate ice particles based on their high-LDR signatures. However, for low-LDR values, the vertical-stare observations cannot be used to distinguish between isometric/spherical shapes and oblate shapes. Using the spectrally resolved approach, it was possible to identify that the prolate, secondary ice particles were formed from slightly to moderately oblate ice crystals. Thus, in the presented case, the reason for the production of the secondary ice does not necessarily need to be rime splintering. Indications are given that the branches of oblate ice crystals, such as dendrites fell off, in addition, which then provided the nuclei for the growth of the secondary columnar ice crystals.

5 Summary & Conclusions

The significance of mixed-phase clouds in mid-latitude precipitation underscores the need for comprehensive study due to their complex microphysical structure. This study was dedicated to investigating the shape of ice particles within such clouds.

Atmospheric
Measurement
Techniques
Open Access
EGU
Discussions

We presented an algorithm, the spectrally resolved shape and orientation retrieval, which builds upon the existing main-peak approach to retrieve multiple hydrometer types in the same volume of air. As the main-peak approach was demonstrated to effectively identify the shape and orientation of primary hydrometer types in stratiform clouds, its limitations are evident when dealing with the diverse range of hydrometeor types characterized by variations in size and Doppler velocity. In the spectrally resolved approach, the Doppler spectrum is divided into five parts, and for each part, the differential reflectivity and correlation coefficient are averaged and compared with modeled values. The result yields five pairs of values of polarizability ratio, indicating shape, and degree of orientation, indicating the orientation, of ice particles.

The ACCEPT campaign, conducted in Cabauw, the Netherlands in 2014, aimed to assess the capabilities of both the main-peak approach and the spectrally resolved approach. Ensuring the reliability of Doppler spectra for analysis is crucial, necessitating the resolution of issues arising from horizontal wind, particularly the folding problem and the horizontal shift of the Doppler spectrum. Our study, through a first case study, demonstrates how the spectrally resolved approach successfully retrieves multiple hydrometeor types, encompassing both oblate and prolate shapes. Furthermore, our research highlights the new approach's effectiveness in identifying secondary ice production in a second case study. Nevertheless, this study provides also evidence that secondary ice formation or ice multiplication processes do not necessarily need to be active when multiple hydrometeor shapes are present within one cloud volume. As the application of the spectrally-resolved shape retrieval demonstrated, prolate particles can also form independent of any seeding by particles from higher/colder levels.

The extended shape and orientation retrieval has the potential to provide information for higher-level retrievals of cloud microphysical properties and for empirical studies of mixed-phase clouds. State-of-the-art cloud microphysical retrievals, such as the one of Bühl et al. (2019) for ice crystal number size distribution rely on the provision of accurate information about the shape of the investigated hydrometeors. Other retrievals, such as DARDAR (Delanoë and Hogan, 2010) or CAPTIVATE (Mason et al., 2023) rely on the presence of only one hydrometeor type in order to provide plausible results. Shape discrimination techniques which can especially also discriminate between isometric and oblate particles, which is hard to be achieved based on vertical-stare observations, are key to constrain these retrievals. In future, the retrievals might be refined in order to obtain precise microphysical properties (number, size, water content) separately for each identified shape class. Last but not least, the availability of polarizability ratio and degree of orientation as quantitative cloud parameters is helpful, since the same parameters can also be obtained from numerical model simulations of clouds, as was previously demonstrated by Welss et al. (2024). In future, simulations of the distribution of the polarizability ratio in a cloud-resolved model will become comparable against their observed counterparts.

Data availability. The vertical-stare observations from the remote sensing instruments are available via https://cloudnet.fmi.fi/site/cabauw. All data which were used for processing and interpretation in the framework of this study can be found at https://doi.org/10.5281/zenodo.14178517 (Hajipour et al., 2024)

.

500 *Author contributions.* MH developed the spectrally-resolved retrieval and authored the majority of the manuscript. PS supervised the retrieval development and contributed to the manuscript writing. HG, KO, AT, MR contributed technical components and datasets to the retrieval and added passages to the manuscript.

Competing interests. The contact author has declared that none of the authors has any competing interests.

References

Althausen, D., Engelmann, R., Baars, H., Heese, B., Ansmann, A., Müller, D., and Komppula, M.: Portable Raman Lidar PollyXT for Automated Profiling of Aerosol Backscatter, Extinction, and Depolarization, Journal of Atmospheric and Oceanic Technology, 26, 2366–2378, https://doi.org/10.1175/2009jtecha1304.1, 2009.

Austin, P. H. and Jeffery, C. A.: Homogeneous nucleation of supercooled water: Results from a new equation of state, https://open.library.ubc.ca/collections/facultyresearchandpublications/52383/items/1.0041772, 1997.

Baars, H., Walchester, J., Basharova, E., Gebauer, H., Radenz, M., Bühl, J., Barja, B., Wandinger, U., and Seifert, P.: Long-term validation of Aeolus L2B wind products at Punta Arenas, Chile, and Leipzig, Germany, Atmospheric Measurement Techniques, 16, 3809–3834, https://amt.copernicus.org/articles/16/3809/2023/, 2023.

Bühl, J., Seifert, P., Wandinger, U., Baars, H., Kanitz, T., Schmidt, J., Myagkov, A., Engelmann, R., Skupin, A., Heese, B., Klepel, A., Althausen, D., and Ansmann, A.: LACROS: the Leipzig Aerosol and Cloud Remote Observations System, in: Remote Sensing of Clouds and the Atmosphere XVIII; and Optics in Atmospheric Propagation and Adaptive Systems XVI, edited by Comeron, A., Kassianov, E. I., Schäfer, K., Stein, K., and Gonglewski, J. D., vol. 8890, p. 889002, International Society for Optics and Photonics, SPIE, https://doi.org/10.1117/12.2030911, 2013.

Bühl, J., Seifert, P., Radenz, M., Baars, H., and Ansmann, A.: Ice crystal number concentration from lidar, cloud radar and radar wind profiler measurements, Atmospheric Measurement Techniques, 12, 6601–6617, https://amt.copernicus.org/articles/12/6601/2019/, 2019.

Caylor, I. J., Goddard, J. W. F., Hopper, S. E., and Illingworth, A. J.: Bright Band Errors in Radar Estimates of Rainfall: Identification and Correction Using Polarization Diversity, pp. 294–303, Springer Netherlands, Dordrecht, https://doi.org/10.1007/978-94-009-0551-1_34, 1990.

Delanoë, J. and Hogan, R. J.: Combined CloudSat-CALIPSO-MODIS retrievals of the properties of ice clouds, Journal of Geophysical Research (Atmospheres), 115, D00H29, https://doi.org/10.1029/2009JD012346, 2010.

Di Girolamo, P., Summa, D., Cacciani, M., Norton, E. G., Peters, G., and Dufournet, Y.: Lidar and radar measurements of the melting layer: observations of dark and bright band phenomena, Atmospheric Chemistry and Physics, 12, 4143–4157, https://acp.copernicus.org/articles/12/4143/2012/, 2012.

Engelmann, R., Kanitz, T., Baars, H., Heese, B., Althausen, D., Skupin, A., Wandinger, U., Komppula, M., Stachlewska, I. S., Amiridis, V., Marinou, E., Mattis, I., Linné, H., and Ansmann, A.: The automated multiwavelength Raman polarization and water-vapor lidar Polly^{XT}: the neXT generation, Atmospheric Measurement Techniques, 9, 1767–1784, https://amt.copernicus.org/articles/9/1767/2016/, 2016.

Field, P. R., Hogan, R. J., Brown, P. R. A., Illingworth, A. J., Choularton, T. W., and Cotton, R. J.: Parametrization of ice-particle size distributions for mid-latitude stratiform cloud, Quarterly Journal of the Royal Meteorological Society, 131, 1997–2017, https://rmets.onlinelibrary.wiley.com/doi/abs/10.1256/qj.04.134, 2005.

Fukao, S. and Hamazu, K.: Radar for Meteorological and Atmospheric Observations, Springer Japan, https://doi.org/10.1007/978-4-431-54334-3, 2014.

Griesche, H. J., Seifert, P., Ansmann, A., Baars, H., Barrientos Velasco, C., Bühl, J., Engelmann, R., Radenz, M., Zhenping, Y., and Macke, A.: Application of the shipborne remote sensing supersite OCEANET for profiling of Arctic aerosols and clouds during amp;lt;iamp;gt;Polarsternamp;lt;/iamp;gt; cruise PS106, Atmospheric Measurement Techniques, 13, 5335–5358, https://doi.org/10.5194/amt-13-5335-2020, 2020.

Guichard, F. and Couvreux, F.: A short review of numerical cloud-resolving models, Tellus A: Dynamic Meteorology and Oceanography, 69, 1373 578, https://doi.org/10.1080/16000870.2017.1373578, 2017.

545 Görsdorf, U., Lehmann, V., Bauer-Pfundstein, M., Peters, G., Vavriv, D., Vinogradov, V., and Volkov, V.: A 35-GHz Polarimetric Doppler Radar for Long-Term Observations of Cloud Parameters—Description of System and Data Processing, Journal of Atmospheric and Oceanic Technology, 32, 675 – 690, https://journals.ametsoc.org/view/journals/atot/32/4/jtech-d-14-00066_1.xml, 2015.

Hajipour, M., Myagkov, A., Seifert, P., Engelmann, R., Holger, B., and Bühl, J.: Case stuides of ground-based remote sensing observations from Cabauw, NL, as obtained during the ACCEPT campaign in 2014., https://doi.org/10.5281/zenodo.14178517, 2024.

550 Hallet, J. and Mossop, S. C.: Production of secondary ice particles during the riming process, Nature, 249, 26–28, https://doi.org/10.1038/249026a0, 1974.

Hoose, C. and Möhler, O.: Heterogeneous ice nucleation on atmospheric aerosols: a review of results from laboratory experiments, Atmospheric Chemistry and Physics, 12, 9817–9854, https://doi.org/10.5194/acp-12-9817-2012, 2012.

Illingworth, A. J., Hogan, R. J., O'Connor, E., Bouniol, D., Brooks, M. E., Delanoé, J., Donovan, D. P., Eastment, J. D., Gaussiat, N.,
555 Goddard, J. W. F., Haeffelin, M., Baltink, H. K., Krasnov, O. A., Pelon, J., Piriou, J.-M., Protat, A., Russchenberg, H. W. J., Seifert, A., Tompkins, A. M., van Zadelhoff, G.-J., Vinit, F., Willén, U., Wilson, D. R., and Wrench, C. L.: Cloudnet: Continuous Evaluation of Cloud Profiles in Seven Operational Models Using Ground-Based Observations, Bulletin of the American Meteorological Society, 88, 883 – 898, https://journals.ametsoc.org/view/journals/bams/88/6/bams-88-6-883.xml, 2007.

Jing, Z. and Wiener, G.: Two-Dimensional Dealiasing of Doppler Velocities, Journal of Atmospheric and Oceanic Technology, 10, 798 –
560 808, https://journals.ametsoc.org/view/journals/atot/10/6/1520-0426_1993_010_0798_tddodv_2_0_co_2.xml, 1993.

Johnson, K., Fairless, T., and Giangrande, S.: Ka-Band ARM Zenith Radar Corrections (KAZRCOR, KAZRCFRCOR) Value-Added Products, https://www.osti.gov/biblio/1647336, 2020.

Kalesse, H., Szyrmer, W., Kneifel, S., Kollias, P., and Luke, E.: Fingerprints of a riming event on cloud radar Doppler spectra: observations and modeling, Atmospheric Chemistry and Physics, 16, 2997–3012, https://doi.org/10.5194/acp-16-2997-2016, 2016.

565 Kollias, P., Clothiaux, E. E., Miller, M. A., Albrecht, B. A., Stephens, G. L., and Ackerman, T. P.: Millimeter-Wavelength Radars: New Frontier in Atmospheric Cloud and Precipitation Research, Bulletin of the American Meteorological Society, 88, 1608 – 1624, https://journals.ametsoc.org/view/journals/bams/88/10/bams-88-10-1608.xml, 2007.

Kollias, P., Clothiaux, E. E., Ackerman, T. P., Albrecht, B. A., Widener, K. B., Moran, K. P., Luke, E. P., Johnson, K. L., Bharad-waj, N., Mead, J. B., Miller, M. A., Verlinde, J., Marchand, R. T., and Mace, G. G.: Development and Applications of ARM
570 Millimeter-Wavelength Cloud Radars, Meteorological Monographs, 57, 17.1 – 17.19, https://journals.ametsoc.org/view/journals/amsm/57/1/amsmonographs-d-15-0037.1.xml, 2016.

Korolev, A. and Leisner, T.: Review of experimental studies of secondary ice production, Atmospheric Chemistry and Physics, 20, 11 767–11 797, https://acp.copernicus.org/articles/20/11767/2020/, 2020.

Korolev, A., McFarquhar, G., Field, P. R., Franklin, C., Lawson, P., Wang, Z., Williams, E., Abel, S. J., Axisa, D., Borrmann, S., Crosier, J.,
575 Fugal, J., Krämer, M., Lohmann, U., Schlenczek, O., Schnaiter, M., and Wendisch, M.: Mixed-Phase Clouds: Progress and Challenges, Meteorological Monographs, 58, 51–550, https://doi.org/10.1175/amsmonographs-d-17-0001.1, 2017.

Küchler, N., Kneifel, S., Löhnert, U., Kollias, P., Czekala, H., and Rose, T.: A W-Band Radar–Radiometer System for Accurate and Continuous Monitoring of Clouds and Precipitation, Journal of Atmospheric and Oceanic Technology, 34, 2375 – 2392, https://journals.ametsoc.org/view/journals/atot/34/11/jtech-d-17-0019.1.xml, 2017.

580   Li, H. and Moisseev, D.: Two Layers of Melting Ice Particles Within a Single Radar Bright Band: Interpretation and Implications, Geophysical Research Letters, 47, e2020GL087 499, https://agupubs.onlinelibrary.wiley.com/doi/abs/10.1029/2020GL087499, e2020GL087499 10.1029/2020GL087499, 2020.

Li, H., Korolev, A., and Moisseev, D.: Supercooled liquid water and secondary ice production in Kelvin–Helmholtz instability as revealed by radar Doppler spectra observations, Atmospheric Chemistry and Physics, 21, 13 593–13 608, https://acp.copernicus.org/articles/21/13593/
585   2021/, 2021.

Luke, E. P., Kollias, P., and Shupe, M. D.: Detection of supercooled liquid in mixed-phase clouds using radar Doppler spectra, Journal of Geophysical Research, 115, https://doi.org/10.1029/2009jd012884, 2010.

Martucci, G. and O'Dowd, C. D.: Ground-based retrieval of continental and marine warm cloud microphysics, Atmospheric Measurement Techniques, 4, 2749–2765, https://amt.copernicus.org/articles/4/2749/2011/, 2011.

590   Mason, S. L., Hogan, R. J., Bozzo, A., and Pounder, N. L.: A unified synergistic retrieval of clouds, aerosols, and precipitation from Earth-CARE: the ACM-CAP product, Atmospheric Measurement Techniques, 16, 3459–3486, https://doi.org/10.5194/amt-16-3459-2023, 2023.

Matrosov: Ice Hydrometeor Shape Estimations Using Polarimetric Operational and Research Radar Measurements, Atmosphere, 11, 97, https://doi.org/10.3390/atmos11010097, 2020.

Matrosov, S. Y.: Theoretical Study of Radar Polarization Parameters Obtained from Cirrus Clouds., Journal of Atmospheric Sciences, 48,
595   1062–1070, https://doi.org/10.1175/1520-0469(1991)048<1062:TSORPP>2.0.CO;2, 1991.

Matsuo, T. and Fukuta, N.: Experimental Study of Ice Crystal Growth below Water Saturation in the University of Utah Supercooled Cloud Tunnel, Papers in Meteorology and Geophysics, 38, 247–264, https://doi.org/10.2467/mripapers.38.247, 1987.

Melnikov and Straka: jtechD1200212 1691..1703, 2013.

Mitchell, D. L.: Use of Mass- and Area-Dimensional Power Laws for Determining Precipitation Particle Terminal Velocities., Journal of
600   Atmospheric Sciences, 53, 1710–1723, https://doi.org/10.1175/1520-0469(1996)053<1710:UOMAAD>2.0.CO;2, 1996.

Myagkov, A., Seifert, P., Wandinger, U., Bauer-Pfundstein, M., and Matrosov, S. Y.: Effects of Antenna Patterns on Cloud Radar Polarimetric Measurements, Journal of Atmospheric and Oceanic Technology, 32, 1813–1828, https://doi.org/10.1175/JTECH-D-15-0045.1, 2015.

Myagkov, A., Seifert, P., Bauer-Pfundstein, M., and Wandinger, U.: Cloud radar with hybrid mode towards estimation of shape and orientation of ice crystals, Atmospheric Measurement Techniques, 9, 469–489, https://amt.copernicus.org/articles/9/469/2016/, 2016a.

605   Myagkov, A., Seifert, P., Wandinger, U., Bühl, J., and Engelmann, R.: Relationship between temperature and apparent shape of pristine ice crystals derived from polarimetric cloud radar observations during the ACCEPT campaign, Atmospheric Measurement Techniques, 9, 3739–3754, https://amt.copernicus.org/articles/9/3739/2016/, 2016b.

Mülmenstädt, J., Sourdeval, O., Delanoë, J., and Quaas, J.: Frequency of occurrence of rain from liquid-, mixed-, and ice-phase clouds derived from A-Train satellite retrievals, Geophysical Research Letters, 42, 6502–6509, https://agupubs.onlinelibrary.wiley.com/doi/abs/
610   10.1002/2015GL064604, 2015.

Pruppacher, H. R., Klett, J. D., and Wang, P. K.: Microphysics of Clouds and Precipitation, Aerosol Science and Technology, 28, 381–382, https://doi.org/10.1080/02786829808965531, 1998.

Qi, C., Prior, D. J., Craw, L., Fan, S., Llorens, M.-G., Griera, A., Negrini, M., Bons, P. D., and Goldsby, D. L.: Crystallographic preferred orientations of ice deformed in direct-shear experiments at low temperatures, The Cryosphere, 13, 351–371, https://tc.copernicus.org/
615   articles/13/351/2019/, 2019.

Radenz, M., Bühl, J., Seifert, P., Griesche, H., and Engelmann, R.: peakTree: a framework for structure-preserving radar Doppler spectra analysis, Atmospheric Measurement Techniques, 12, 4813–4828, https://doi.org/10.5194/amt-12-4813-2019, 2019.

Atmospheric
Measurement
Techniques
Discussions

Open Access

EGU

Ray, P. S. and Ziegler, C.: De-Aliasing First-Moment Doppler Estimates, Journal of Applied Meteorology and Climatology, 16, 563 – 564, https://journals.ametsoc.org/view/journals/apme/16/5/1520-0450_1977_016_0563_dafmde_2_0_co_2.xml, 1977.

620   Rose, T., Crewell, S., Löhnert, U., and Simmer, C.: A network suitable microwave radiometer for operational monitoring of the cloudy atmosphere, Atmospheric Research, 75, 183–200, https://doi.org/10.1016/j.atmosres.2004.12.005, 2005.

Ryzhkov, A. V., Schuur, T. J., Burgess, D. W., Heinselman, P. L., Giangrande, S. E., and Zrnic, D. S.: The Joint Polarization Experiment: Polarimetric Rainfall Measurements and Hydrometeor Classification, Bulletin of the American Meteorological Society, 86, 809 – 824, https://journals.ametsoc.org/view/journals/bams/86/6/bams-86-6-809.xml, 2005.

625   Seliga, T. A. and Bringi, V. N.: Potential Use of Radar Differential Reflectivity Measurements at Orthogonal Polarizations for Measuring Precipitation, Journal of Applied Meteorology and Climatology, 15, 69 – 76, https://journals.ametsoc.org/view/journals/apme/15/1/1520-0450_1976_015_0069_puordr_2_0_co_2.xml, 1976.

Shupe, M. D., Kollias, P., Matrosov, S. Y., and Schneider, T. L.: Deriving Mixed-Phase Cloud Properties from Doppler Radar Spectra, Journal of Atmospheric and Oceanic Technology, 21, 660 – 670, https://journals.ametsoc.org/view/journals/atot/21/4/1520-0426_2004_021_0660_dmcpfd_2_0_co_2.xml, 2004.

630   Suortti, T. M., Kivi, R., Kats, A., Yushkov, V., Kämpfer, N., Leiterer, U., Miloshevich, L. M., Neuber, R., Paukkunen, A., Ruppert, P., and Vömel, H.: Tropospheric Comparisons of Vaisala Radiosondes and Balloon-Borne Frost-Point and Lyman-α Hygrometers during the LAUTLOS-WAVVAP Experiment, Journal of Atmospheric and Oceanic Technology, 25, 149–166, https://doi.org/10.1175/2007jtecha887.1, 2008.

635   Teisseire, A., Seifert, P., Myagkov, A., Bühl, J., and Radenz, M.: Determination of the vertical distribution of in-cloud particle shape using SLDR-mode 35 GHz scanning cloud radar, Atmospheric Measurement Techniques, 17, 999–1016, https://amt.copernicus.org/articles/17/999/2024/, 2024.

Trömel, S., Simmer, C., Blahak, U., Blanke, A., Doktorowski, S., Ewald, F., Frech, M., Gergely, M., Hagen, M., Janjic, T., Kalesse-Los, H., Kneifel, S., Knote, C., Mendrok, J., Moser, M., Köcher, G., Mühlbauer, K., Myagkov, A., Pejcic, V., Seifert, P., Shrestha, P., Teisseire, A., von Terzi, L., Tetoni, E., Vogl, T., Voigt, C., Zeng, Y., Zinner, T., and Quaas, J.: Overview: Fusion of radar polarimetry and numerical atmospheric modelling towards an improved understanding of cloud and precipitation processes, Atmospheric Chemistry and Physics, 21, 17 291–17 314, https://acp.copernicus.org/articles/21/17291/2021/, 2021.

Tukiainen, S., O'connor, E., and Korpinen, A.: CloudnetPy: A Python package for processing cloud remote sensing data, Journal of Open Source Software, 5, 2123, 2020.

645   Verlinde, J., Rambukkange, M. P., Clothiaux, E. E., McFarquhar, G. M., and Eloranta, E. W.: Arctic multilayered, mixed-phase cloud processes revealed in millimeter-wave cloud radar Doppler spectra, Journal of Geophysical Research: Atmospheres, 118, 13,199–13,213, https://agupubs.onlinelibrary.wiley.com/doi/abs/10.1002/2013JD020183, 2013.

Wakasugi, K., Mizutani, A., Matsuo, M., Fukao, S., and Kato, S.: A Direct Method for Deriving Drop-Size Distribution and Vertical Air Velocities from VHF Doppler Radar Spectra, Journal of Atmospheric and Oceanic Technology, 3, 623 – 629, https://journals.ametsoc.org/view/journals/atot/3/4/1520-0426_1986_003_0623_admfdd_2_0_co_2.xml, 1986.

650   Welss, J., Siewert, C., and Seifert, A.: Explicit Habit-Prediction in the Lagrangian Super-Particle Ice Microphysics Model McSnow, Journal of Advances in Modeling Earth Systems, 16, https://doi.org/10.1029/2023ms003805, 2024.

Westbrook, C. D., Illingworth, A. J., O'Connor, E. J., and Hogan, R. J.: Doppler lidar measurements of oriented planar ice crystals falling from supercooled and glaciated layer clouds, Quarterly Journal of the Royal Meteorological Society, 136, 260–276, https://rmets.onlinelibrary.wiley.com/doi/abs/10.1002/qj.528, 2010.

Zeng, X., Ulanowski, Z., Heymsfield, A. J., Wang, Y., and Li, X.: Stability Analysis of Ice Crystal Orientation, Journal of the Atmospheric Sciences, 80, 1621 – 1633, https://journals.ametsoc.org/view/journals/atsc/80/6/JAS-D-22-0223.1.xml, 2023.